A Novel Approach for 3-D Imaging of Ships With SAR Systems Based on 3-DOF Micro-Doppler Frequencies

Peng Zhou, *Senior Member, IEEE*, Jichen Wu, Chuwen Cao, Xi Zhang, Zhenhua Zhang, Genwang Liu, and Jie Zhang

***Abstract*—To address the urgent need to improve the ship type discrimination capability in maritime target detection, this article explores synthetic aperture radar (SAR) three-dimensional (3-D) imaging of moving ships, which can provide high robustness and stability of 3-D structural characteristics for ship type discrimination. This paper defines the three-degree-of-freedom (3-DOF) micro-Doppler frequency of ship scatterers, specifically referring to the Doppler frequency caused by the three-axis rotation of the ship when the motion of the radar platform and the ship's planar motion are both compensated. The 3-DOF micro-Doppler frequency of the ship scatterers is closely related to the roll, pitch, and yaw three-axis rotation parameters of the ship and contains the 3-D coordinate information of the scatterers. Building upon the high-precision extraction of the 3-DOF micro-Doppler frequency of ship scatterers, this paper proposes an SAR 3-D imaging method for moving ships based on this frequency. The proposed method describes the ship's rotational characteristics using 27 parameters and converts the variation in the 3-DOF micro-Doppler frequency of the scatterer into a set of weighted coefficients of B-spline basis functions. Two long short-term memory networks are constructed to estimate the 27 parameters describing the ship's rotation and invert the 3-D coordinates of the scatterers. Finally, through the processing of simulated and experimental data, the feasibility of using the 3-DOF micro-Doppler frequency of ship scatterers to achieve high-precision estimation of the ship's three-axis rotation parameters and high-precision inversion of 3-D coordinates was verified.**

***Index Terms*—3-D imaging of ships, estimation of ship three-axis rotation parameters, long short-term memory (LSTM) networks, multivariate nonlinear optimization model.**

I. Introduction

THE detection, classification, and recognition of ship targets at sea are important applications of ocean remote sensing [1]. Synthetic aperture radar (SAR) imaging technology is an important technical means for classifying and identifying marine vessels. However, misjudgment still occurs fairly frequently when SAR images are used for ship type discrimination. This is mainly due to the fact that SAR systems are designed for stationary scenarios, whereas ships traveling on the sea sway and rotate in the three axial directions of roll, pitch, and yaw in addition to their translational motion. As a result, severe distortions such as displacement, size distortion, and blurring occur the SAR images of ships. This makes it difficult to achieve accurate discrimination of ship types solely using two-dimensional (2-D) SAR image information. The 3-D structure of ship targets is a highly robust and stable feature. To improve the discrimination ability of ship types, the development of SAR 3-D imaging technology for moving ships is urgently needed. However, similar to the 2-D SAR technology, existing SAR 3-D imaging technologies are designed for imaging still scenes, and problems such as image blurring and ship structure distortion occur when these technologies are applied to imaging of moving ships. Thus, the three-degree-of-freedom (3-DOF) swaying and rotation of ships is the fundamental reason for the poor quality of images obtained when the existing SAR 3-D imaging technology is applied to ship imaging. On the other hand, the micro-Doppler frequency caused by the 3-DOF swaying and rotation of ships includes the rotation parameters and geometric structure information of ships [2], [3]. Clearly, accurate estimation of the three-axis rotation parameters of a ship using the 3-DOF micro-Doppler frequency is very important for achieving 3-D imaging of moving ships.

Due to the complexity of their motion, it is very difficult to obtain high-quality 3-D images of micromoving targets, and the estimation of the motion parameters of micromoving targets has

Manuscript received 11 May 2024; revised 16 June 2024; accepted 5 July 2024. Date of publication 9 July 2024; date of current version 24 July 2024. This work was supported in part by the Qingdao Science and Technology Benefiting the People Demonstration Project under Grant 24-1-8-cspz-5-nsh, in part by the Key Funds of National Natural Science Foundation of China under Grant 61931025, in part by the Key Program of Joint Fund of the National Natural Science Foundation of China and Shandong Province under Grant U22A20586, and in part by the National Natural Science Foundation of China under Grant 42106177. *(Corresponding author: Peng Zhou.)*

Peng Zhou is with the College of Oceanography and Space Informatics, China University of Petroleum, Qingdao 266580, China, and also with the Technology Innovation Center for Maritime Silk Road Marine Resources and Environment Networked Observation, Ministry of Natural Resources, Qingdao 266580, China (e-mail: zhoupeng@upc.edu.cn).

Jichen Wu is with the College of Oceanography and Space Informatics, China University of Petroleum, Qingdao 266580, China.

Chuwen Cao is with the Yantai Branch, China United Network Communications Group Company Ltd., Yantai 264001, China.

Xi Zhang and Genwang Liu are with the First Institute of Oceanography, Ministry of Natural Resources of the People's Republic of China, Qingdao 266061, China.

Zhenhua Zhang is with the School of Astronautics, Beihang University, Beijing 100191, China.

Jie Zhang is with the College of Oceanography and Space Informatics, China University of Petroleum, Qingdao 266580, China, also with the Technology Innovation Center for Maritime Silk Road Marine Resources and Environment Networked Observation, Ministry of Natural Resources, Qingdao 266580, China, and also with the First Institute of Oceanography, Ministry of Natural Resources of the People's Republic of China, Qingdao 266061, China.

Digital Object Identifier 10.1109/JSTARS.2024.3425657

also become a focus of research. To date, several methods for estimating the rotational parameters of micromoving targets, including the high-resolution range profile, image processing, and multiangle observation methods have been developed. For broadband imaging radar, due to its high range resolution, the amplitude of target radial micromotion is generally significantly greater than that of the range resolution unit. Therefore, the echoes after translation compensation appear as multiple range slow-time plane curves corresponding to the radial micromotion history of each scatterer in the high-resolution range profile. Zhou et al. [4] proposed the coherent single-range Doppler interferometry-modified general parameterized time-frequency algorithm to extract the micro-Doppler frequency curve of conical targets and then estimated parameters such as the spin velocity and precession velocity that characterize the micro dynamic characteristics of the target based on the extracted micro-Doppler frequency curve. Notably, this method obtains only range profiles from a single perspective to estimate motion parameters, resulting in low estimation accuracy. Image processing methods first obtain ship images through radar imaging algorithms and then extract feature quantities from the images and use them to estimate the three-axis rotation parameters of the ship [5]. Cao et al. [6] used the inverse synthetic aperture radar (ISAR) imaging algorithm to obtain the imaging projection plane of a ship and then fitted the ship centerline slope and ISAR image Doppler broadening and other feature variables. Finally, based on Doppler broadening, the rotations at different imaging times were displayed, and the ship's three-axis rotation parameters were estimated. However, for single-channel radar, the rotational component of the target scatterer in the direction of the radar line of sight around the rotation axis does not cause a change in the instantaneous range between the radar and the scatterer, and the corresponding Doppler frequency is zero. Therefore, it is impossible to measure the rotational component of the target in the direction of the radar line of sight, resulting in a low estimation accuracy of the ship's three-axis rotational parameters. The method based on multiangle observation utilizes the diversity of angles observed by distributed radar or multiple sensors when observing the same target to estimate the angular velocity components of pitch, yaw, and roll. Santi et al. [7], [8] used distributed ISAR to observe moving ships, extracted significant scatterers from echo data obtained by multiple receivers, correlated them, built a maximum likelihood estimator and Doppler-matching estimator, and estimated the three-axis rotational angular velocity of ships in terms of the roll, pitch, and yaw. Although such methods have improved the estimation accuracy of rotational parameters in a short period, methods for multiangle observation have not accounted for the time-varying three-axis rotational angular velocity, resulting in lower estimation accuracy. The studies described above indicate that development of a method that can accurately estimate the three-axis rotation parameters of the time-varying roll, pitch, and yaw of ships is challenging.

Research specifically focusing on the inversion of 3-D coordinates for micromotion targets has been relatively scarce. Currently, the methods mainly employed for 3-D imaging include those based on SAR-derived Doppler parameter estimation, interferometric processing, and dual/multiradar methods. SAR-based Doppler parameter estimation methods correlate the azimuth and elevation coordinates of the scatterers with the Doppler center frequency and frequency modulation slope of the scatterers, achieving 3-D image reconstruction of ships by estimating the Doppler center frequency and the frequency modulation slope of each scatterer [9], [10], [11]. However, when the accumulation time of the target is relatively long (e.g., typical accumulation times for high-resolution airborne SAR and spaceborne spotlight SAR are generally several seconds or longer), we find that the instantaneous Doppler frequency of ship scatterers does not satisfy the assumption of linear frequency modulation [12]. Therefore, using SAR-based Doppler parameter estimation methods for scatterer coordinate inversion will lead to significant reconstruction errors. Additionally, the proportionality coefficient between the Doppler parameters of the scatterers and their coordinates is related to the rotation of the target ship [13]. Since prior information regarding the rotation of target ships is usually unknown, the coordinates inferred by the above method are not the true coordinates of the scatterers. The method based on interference processing involves the installation of three L-shaped antennas on the platform to form two mutually perpendicular baselines. By performing interference processing on two ISAR images generated on the same baseline, the projection values of the scatterer coordinates in the corresponding baseline direction are obtained. Combined with the slant range coordinate information obtained after range compression, inverted 3-D coordinates can be obtained [14]. Zhang et al. [15] proposed a phase correction method to maintain complete interferometric phase information and reconstruct 3-D images of ships. However, due to the need to install L-shaped or more complex antennas on the platform, current interference processing methods are generally applied only to ground-based radar. In 3-D imaging methods based on dual/multibase radars, multiple radars from different perspectives are utilized to measure the differences in the target features, and 3-D images of the target are obtained through correlation processing. Ai et al. [16] used T/R-T bistatic radar to establish a bistatic echo signal model for rotating targets and achieved imaging of rotating targets based on the connection between single and bistatic echoes of the same scatterer and Hough transform. Under ideal conditions, this type of method can be used to effectively invert the 3-D coordinates of scatterers. However, in practical applications, the anisotropy of the target scattering center and the mutual occlusion between scatterers complicate the joint processing of radar echoes, and further research is needed to apply this method in practical use.

In this article, a 3-D imaging method based on a 3-DOF micro-Doppler frequency is proposed to address the difficulties facing existing methods in high-precision imaging of ships with 3-DOF sway and rotation. First, the algorithm for estimating significant scatterers on ships is studied. By using the 3-DOF micro-Doppler frequency, the instantaneous distance change matrix between the scattering center of the scatterer and the antenna phase center can be established, and the change matrix can be

subsequently used to invert the 3-D coordinates of several significant scatterers. Then, an algorithm for estimating the three-axis rotation parameters of ships is developed. Due to the complex nonlinear relationship between the micro-Doppler frequency of the scatterer and the 3-D coordinates of the scatterer, the three-axis rotation parameters of the ship, and the 3-D coordinates of the antenna phase center, it is difficult to find a specific function expression. Therefore, utilizing the property that any nonlinear function can be described by a generalized linear regression equation, a linear combination of B-spline basis functions and coefficients corresponding to significant scatterers can be used to represent the micro-Doppler frequency, and the coefficient matrix can be subsequently solved using the recursive least squares principle. Second, a multivariate optimization model solution method based on a long short-term memory (LSTM) neural network is studied to explore the relationships between the coefficient matrix and the amplitude, period, and initial phase parameters of the rotational angular velocity on the antenna phase center, ship roll, yaw, and pitch axes. Ultimately, three sets of amplitude and initial phase parameters of the rotational angular velocity for the time-varying ship roll, yaw, and pitch axes are obtained via high-precision estimation of 27 parameters, including the period and initial phase. Finally, a multivariate nonlinear optimization model is established for inverting the 3-D coordinates of ship scatterers, and the 3-D coordinates of all scatterers are inverted. The estimation accuracy of the method proposed in this paper is verified through simulation and experimental testing, demonstrating its effectiveness.

The rest of this article is organized as follows. In Section II, the characteristics of the three-axis rotational angular velocity of a ship are analyzed, and the relationship between the ship's micro-Doppler frequency and rotational angular velocity is established. In Section III, the 3-D coordinate inversion method for significant scatterers on ships is introduced, and a detailed introduction to the estimation method of ship three-axis rotation parameters based on the micro-Doppler frequency, as well as the 3-D imaging method of ships, is provided. Moreover, the algorithm of the method is summarized. In Section IV, the simulation and measured data processing results are presented, and the estimation accuracy of the rotational parameters and the 3-D imaging accuracy of ships are analyzed to verify the accuracy of the method proposed in this article. Finally, Section V provides a summary of this article.

II. Modeling of the Ship 3-DOF Micro-Doppler Model

The ship studied in this article consists of scatterers that are subjected to a 3-DOF rocking rotation in response to waves. The 3-DOF micro-Doppler frequency in this paper refers to the instantaneous Doppler frequency variations in the scatterers caused by the 3-DOF oscillation rotation of the ship during roll, pitch, and yaw.

The geometric model of the motion system is shown in Fig. 1. The coordinate system XYZ is the radar coordinate system E_r, and the origin o is the projection of the radar on the ground plane at the imaging center moment. The X-axis points in the direction of platform flight, the Y-axis points in the direction of

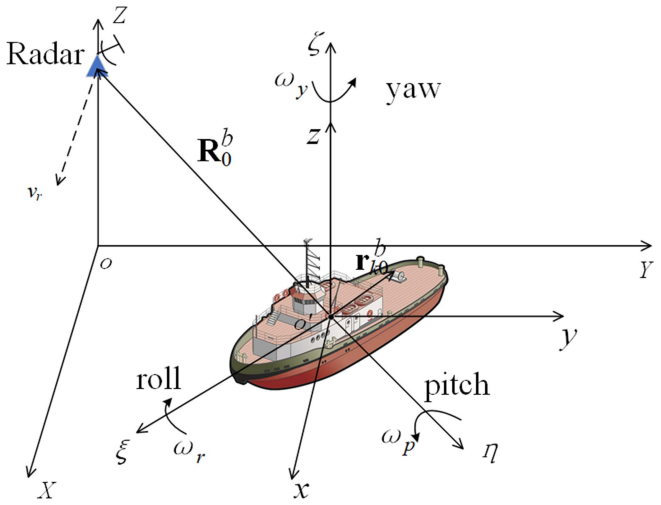

Fig. 1. Geometric model of the system.

counterclockwise rotation by 90° of the X-axis, and the Z-axis points vertically upward. The coordinate system xyz is the ship reference coordinate system E_f, whose axes are defined in the same manner as those of the coordinate system XYZ, except that the rotation center of the ship is chosen as the origin. The coordinate system $\xi\eta\zeta$ is the ship's body coordinate system E_b at the central moment, where the ξ axis points in the bow direction at the imaging central moment, the η axis points in the port side direction of the ship at the central moment of imaging, and the direction of the ζ axis is determined by the right-hand rule. For simplicity, it is assumed that the change between E_b and E_f is given by only a rotation around the z-axis, so that the direction of the ζ-axis coincides with that of the z-axis. ω_r, ω_p, and ω_y represent the angular velocities of the ship's rotations for the roll, pitch, and yaw axes, respectively. v_r indicates the flight speed of the radar platform, $\mathbf{R}_0^b$ denotes the position vector from the rotation center of the ship to the radar defined in the coordinate system E_b, and $\mathbf{r}_{k0}^b$ is the position vector of the kth scatterer at the imaging center moment.

For a scatterer on the ship shown in Fig. 1, rolling, pitching, or yawing with 3-DOF will cause the scatterer to rotate relative to the center of rotation of the ship, resulting in a continuous change in the instantaneous Doppler frequency of the scatterer. According to the relevant classic theories of ship hydrodynamics, the variation law of the ship three-axis rotational angular velocity approximately satisfies the cosine function law [17]. However, previous studies have shown that a single cosine function cannot be used to accurately describe the variation law of three-axis rotation. In particular, when the accumulation time is long, the error is large. Therefore, in this article, the cosine sum function is innovatively used to describe the three-axis rotational angular velocity; that is, the rotational angular velocity and angle corresponding to the roll, pitch, and yaw rotation of the ship at time t can be expressed as follows:

$$\omega_i = A_i \cos\left(\frac{2\pi}{T_i}t + \varphi_i\right) + A_i' \cos\left(\frac{2\pi}{T_i'}t + \varphi'_i\right) + A_i'' \cos\left(\frac{2\pi}{T_i''}t + \varphi''_i\right), i = \text{roll, pitch, yaw} \quad (1)$$

where A_i, A_i', A_i'' are the amplitudes of the rotation, T_i, T_i', T_i'' are the periods of the rotation, and $\varphi_i, \varphi'_i, \varphi''$ are the initial phases.

The rotation matrices of the ship corresponding to the yaw, roll and pitch can be expressed as follows [18], [19]:

$$\boldsymbol{Yaw}\left[\theta_y(t)\right] = \begin{bmatrix} \cos\theta_y(t) & -\sin\theta_y(t) & 0 \\ \sin\theta_y(t) & \cos\theta_y(t) & 0 \\ 0 & 0 & 1 \end{bmatrix} \tag{2}$$

$$\boldsymbol{Roll}\left(\theta_r(t)\right) = \begin{bmatrix} 1 & 0 & 0 \\ 0 & \cos\theta_r(t) & -\sin\theta_r(t) \\ 0 & \sin\theta_r(t) & \cos\theta_r(t) \end{bmatrix} \tag{3}$$

$$\boldsymbol{Pitch}\left(\theta_p(t)\right) = \begin{bmatrix} \cos\theta_p(t) & 0 & \sin\theta_p(t) \\ 0 & 1 & 0 \\ -\sin\theta_p(t) & 0 & cos\theta_p(t) \end{bmatrix} \tag{4}$$

where $\theta_y(t)$, $\theta_p(t)$, and $\theta_r(t)$ represent the rotation angles corresponding to the yaw, pitch and roll at time t, respectively.

The composite rotation matrix of the ship can be expressed as follows:

$$\begin{aligned} &Rot\left[\theta_r(t), \theta_p(t), \theta_y(t)\right] \\ &= \boldsymbol{Roll}\left[\theta_r(t)\right] \cdot \boldsymbol{Pitch}\left[\theta_p(t)\right] \cdot \boldsymbol{Yaw}\left[\theta_y(t)\right]. \end{aligned} \tag{5}$$

When the ship rotates only from zero to the instantaneous time t, scatterer k rotates from the initial coordinate $\mathbf{r}_{k0} = (\xi_{k0}, \eta_{k0}, \zeta_{k0})^T$ to $\mathbf{r}_{kt} = (\xi_{kt}, \eta_{kt}, \zeta_{kt})^T$ in the E_b coordinate system. The relationship between these two position vectors can be expressed as follows:

$$\mathbf{r}_{kt} = \begin{bmatrix} \xi_{kt} \\ \eta_{kt} \\ \zeta_{kt} \end{bmatrix} = Rot\left[\theta_r(t), \theta_p(t), \theta_y(t)\right] \cdot \begin{bmatrix} \xi_{k0} \\ \eta_{k0} \\ \zeta_{k0} \end{bmatrix} \tag{6}$$

The radial velocity of scatterer k relative to the radar can be expressed as follows:

$$v_{kr}(t) = \left[\boldsymbol{\omega}_i(t) \times \mathbf{r}_{kt}\right] \cdot \mathbf{i}_{R0} \tag{7}$$

where $\boldsymbol{\omega}_i(t)$ is the time-varying angular velocity vector of the ship and $\mathbf{i}_{R0}$ is the unit vector corresponding to $\mathbf{R}_0^b$.

When the accumulation time is relatively short (the synthetic aperture time is less than or equal to 1 s), the angle of the three-axis rotation can be ignored. By substituting (6) into (7), the analytical expression for the instantaneous Doppler frequency of the scatterer can be approximated as follows [12]:

$$f_{dk}(t) \approx \frac{2}{\lambda} \cdot \begin{bmatrix} (\eta_{k0} m_3 - \zeta_{k0} m_2) \cdot \omega_r \\ +(\zeta_{k0} m_1 - \xi_{k0} m_3) \cdot \omega_p \\ +(\xi_{k0} m_2 - \eta_{k0} m_1) \cdot \omega_y \end{bmatrix} \tag{8}$$

where m_1, m_2, and m_3 are the 3-D coordinates of the unit vector corresponding to $\mathbf{R}_0^b$.

III. 3-D Imaging Approach for Ships Based on 3-DOF Micro-Doppler Frequencies

A. 3-D Coordinate Inversion Method for Significant Scatterers From a Ship

Investigations of inversion must first be conducted for the 3-D coordinates of several significant scatterers to provide auxiliary information for the estimation of the ship's rotation parameters. In this article, the 3-DOF micro-Doppler frequency extracted from paper [12] is used to establish a change matrix of the instantaneous distance between the scattering center of the scatterer and the antenna phase center, namely, the scattering center trajectory matrix. The change matrix is used to invert the 3-D coordinates of several significant scatterers.

The relationship between the scattering center trajectory matrix and the 3-D coordinates of significant scatterers can be expressed as follows:

$$\mathbf{TR} = \mathbf{RO}_{Na\times 3} \cdot \mathbf{S}_{3\times P'} \tag{9}$$

where $\mathbf{TR}$ is the scattering center track matrix, Na is the number of azimuthal sampling points, $\mathbf{RO}$ is the radar rotation matrix and $\mathbf{S}$ is the matrix consisting of the 3-D coordinates of the P' significant scatterers. Using singular value decomposition, the track matrix can be decomposed as follows:

$$\mathbf{TR}_{\mathrm{Na}\times P'} = \mathbf{U}_{\mathrm{Na}\times\mathrm{Na}} \sum\nolimits_{\mathrm{Na}\times P'} \mathbf{V}^T_{P'\times P'}. \tag{10}$$

The first three singular values of the matrix Σ are relatively large, while the remaining singular values are close to zero and can therefore be approximated as follows:

$$\begin{aligned} \mathbf{TR}_{\mathrm{Na}\times P'} &= \left[(\mathbf{U}_1)_{\mathrm{Na}\times 3} \quad (\mathbf{U}_2)_{\mathrm{Na}\times(\mathrm{Na}-3)}\right] \times \begin{bmatrix} (\sum_1)_{3\times 3} & 0 \\ 0 & 0 \end{bmatrix} \\ &\quad \times \begin{bmatrix} (\mathbf{V}_1)_{3\times P'} \\ (\mathbf{V}_2)_{(P'-3)\times P'} \end{bmatrix} \\ &\approx (\mathbf{U}_1)_{\mathrm{Na}\times 3} \times \left[\left(\sum\nolimits_1\right)_{3\times 3} \times (\mathbf{V}_1)_{3\times P'}\right] = \mathbf{RO'}_{\mathrm{Na}\times 3} \times \mathbf{S'}_{3\times P'}. \end{aligned} \tag{11}$$

In (11), the correlation matrix satisfies the following relationship:

$$\begin{cases} \mathbf{RO'}_{\mathrm{Na}\times 3} = (\mathbf{U}_1)_{\mathrm{Na}\times 3} \\ \mathbf{S'}_{3\times P'} = (\sum\nolimits_1)_{3\times 3} \times (\mathbf{V}_1)_{3\times P'} \end{cases} \tag{12}$$

Clearly, the relationships between $\mathbf{RO}$, $\mathbf{S}$ and $\mathbf{RO'}$, $\mathbf{S'}$can be expressed as follows:

$$\begin{aligned} &\mathbf{RO}_{Na\times 3} \times \mathbf{S}_{3\times P'} \\ &= \left(\mathbf{RO'}_{Na\times 3} \times \mathbf{A}_{3\times 3} \times \mathbf{B}_{3\times 3}\right) \times \left(\mathbf{B}^T_{3\times 3} \times \mathbf{A}^{-1}_{3\times 3} \times \mathbf{S'}_{3\times P'}\right) \end{aligned} \tag{13}$$

where $\mathbf{A}$ is the invertible matrix to be determined and $\mathbf{B}$ is the orthogonal matrix to be determined. By utilizing the property that the modulus of each row in matrix $\mathbf{RO}$ is 1, the least squares estimate $\hat{\mathbf{A}}$ of matrix $\mathbf{A}$ can be obtained. The estimated value $\hat{\mathbf{B}}$ of matrix $\mathbf{B}$ can be obtained using the method provided in [14]. Therefore, the following equations can be obtained:

$$\begin{cases} \widehat{\mathbf{RO}}_{\mathrm{Na}\times 3} = \mathbf{RO'}_{\mathrm{Na}\times 3} \times \hat{\mathbf{A}}_{3\times 3} \times \hat{\mathbf{B}}_{3\times 3} \\ \hat{\mathbf{S}}_{3\times P'} = \hat{\mathbf{B}}^T_{3\times 3} \times \mathbf{A}^{-1}_{3\times 3} \times \mathbf{S'}_{3\times P'} \end{cases} \tag{14}$$

where $\hat{\mathbf{S}}$ is the final estimated 3-D coordinate of the P' significant scatterers. Notably, the number of significant scatterers should be no less than four and they should not be coplanar in order to provide auxiliary information for the estimation of the vessel's three-axis rotation parameters.

B. Estimation of the Time-Varying Ship Three-Axis Rotation Parameters Based on an LSTM Neural Network

1) Modeling of the Multiple Linear Regression Model: Due to the complex nonlinear relationship between the micromotion frequencies of the scatterers and their 3-D coordinates, the three-axis rotation parameters of ships, and the 3-D coordinates of antenna phase centers, solving a mathematical model of the three-axis rotation parameters of a ship is difficult. Therefore, in this article, based on the theory of regression analysis, we use the property that any nonlinear function can be described by a generalized linear regression equation. The mathematical model of the ship's three-axis rotation parameters can be transformed into a linear formula expressed as follows:

$$f_{d,j}(t) = \sum_{l_B=1}^{L_B} W_{jl_B} P_{l_B}(t) \quad j = 1, \ldots, P' \tag{15}$$

where $P_l(t)$ is the selected basis function, L_B is the number of basis functions, W_{jl_B} is the coefficient of $P_{l_B}(t)$ corresponding to the jth significant scatterer, and $f_{d,j}(t)$ is the instantaneous Doppler frequency of the jth significant scatterer calculated using the method provided in [12].

The commonly used estimation methods for nonlinear regression functions include local polynomials [20], Bessel curves [21], and spline methods [22], [23]. However, due to the use of point-by-point fitting in the local polynomial estimation methods, the computational burden increases when the data volume is large, which can easily lead to errors. Moreover, in the local polynomial method, it is assumed that the function is differentiable everywhere, which is difficult to satisfy in many cases. The Bezier curve has significant limitations due to its lack of local modification. Moreover, the use of the Bezier curve also faces a problem of increasing data volumes and calculation errors. Additionally, due to the smoother Bezier curve, the connection is more complex. Therefore, in this article, the B-spline basis function [24], which has the advantages of local modification, high stability, fast convergence and a wide application range, is adopted.

The time series is set to $T_B = \{t_0, t_1, \ldots t_M\}$, and the size of T_B is set to be equal to the synthetic aperture time T_{syn} and satisfies $t_i <= t_{i+1}$ and $i = 1, \ldots, M-1$. Here, t_i represents the knot, M represents the multiplicity of the knot, and T_B represents the knot vector. Then, $P_{i,N}(t)$ is used to represent the Bi Nth B-spline basis function, defined as follows [24], [25]:

$$\begin{cases} P_{i,0}(t) = \begin{cases} 1 & t \in [t_{Bi}, t_{Bi+1}) \\ 0 & \text{otherwise} \end{cases} \\ P_{i,N}(t) = \frac{t-t_i}{t_{i+N}-t_i} P_{i,N-1}(t) + \frac{t_{i+N+1}-t}{t_{i+N+1}-t_{i+1}} P_{i+1,N-1}(t) \end{cases} \tag{16}$$

where $[t_i, t_{i+1})$ is the ith nodal interval and N represents the degree of the basis function. When $N > 0$, $P_{i,N}(t)$ is a linear combination of two $N-1$ order basis functions.

The formula of the B-spline basis functions can be used to determine their desirable properties. Within each interval defined by the knots, B-spline basis functions are infinitely differentiable. At the knots, the basis functions are $N - M$ times continuously differentiable. Therefore, increasing the degree of the basis function improves the continuity of the B-spline curve, while increasing the knot multiplicity reduces continuity. Additionally, if $t \notin [t_i, t_{i+1})$, then $P_{i,N}(t) = 0$, indicating excellent local modification characteristics. For all Bi, N, and t, $P_{i,N}(t) \geq 0$.

After obtaining the basis functions of the generalized linear regression equation using the B-spline basis function method, the next step is to solve for the coefficients of the basis functions. The basis functions from (16) can be substituted into (15), and (15) can be discretized. k represents the discrete time, and K_s represents the number of sampling points. Since (15) involves the unmeasurable coefficient matrix W, we adopt the recursive least squares method [26] to derive the coefficient matrix. The underlying idea of this method is to first calculate the new observed data using (15). Based on the estimated values of the previous moment's observations, the old observed values are corrected using the new observed data according to the recursive algorithm, resulting in new estimated data. As new observed data are successively introduced, parameter estimation is performed sequentially until the estimation error of the parameters reaches the specified range. By applying the principle of recursive least squares, the following recursive formula for the coefficients can be derived [27], [28], [29]:

$$\begin{aligned} W_j(k+1) &= W_j(k) + D_j(k) \cdot \left[f_{d,j}(k) - W_j^T(k) P_j(k) \right] \\ &= W_j(k) + D_j(k) \cdot e_j(k) \end{aligned} \tag{17}$$

$$D_j(k) = \frac{B_j(k) P_j(k)}{1 + P_j^T(k) B_j(k) P_j(k)} \tag{18}$$

$$\begin{aligned} B_j(k+1) &= I - D_j(k) P_j^T(k) S_j(k) \\ k &= 0, 1, \ldots, K_s - 1 \end{aligned} \tag{19}$$

where W_j is the coefficient vector with dimensions of $L_B \times 1$, P_j is the basis function vector with dimensions of $L_B \times 1$, D_j and B_j are the auxiliary vectors and auxiliary matrices with dimensions of $L_B \times 1$ and $L_B \times L_B$, respectively, I is the identity matrix with dimensions of $L_B \times L_B$, and $e_j(k)$ is the error. We let $S_j(0) = \beta_w I$ (where β_w is a sufficiently large positive number). Additionally, we randomly generate $W_j(0)$. By iteratively applying (17) to (19), the coefficient matrix is updated. After calculating K_s data points, we determine whether the loss function $J = \sum_{k=0}^{K_s-1} |e_j(k)^2|$ meets the requirements. If the requirements are met, the calculation ends; otherwise, the process continues to the next iteration.

2) LSTM Neural Network Modeling: The B-spline basis function and the recursive least squares method are used to solve the multivariate optimization model to obtain the basis functions and the correlation coefficient matrix representing the micro-Doppler frequency of the ship scatterers. However, the relationships between the basis functions and the 3-D coordinates of the scatterers and the three-axis rotation parameters of the ship are complex. It is necessary to use neural networks that are suitable for describing complex systems to achieve high-precision estimation of the three-axis rotation parameters of the ship's roll, pitch, and yaw.

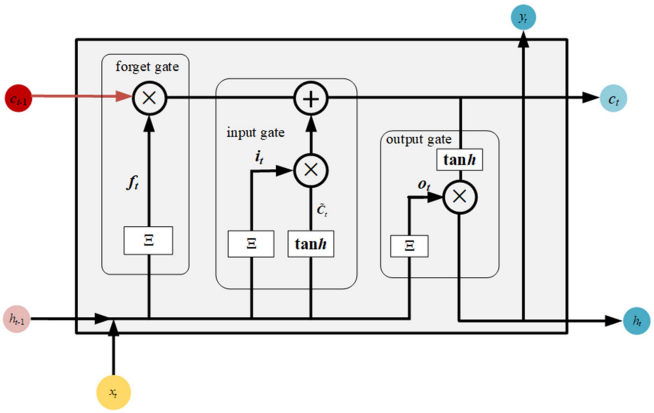

Fig. 2. Internal structure of the LSTM unit.

To date, many applications of neural networks for ship prediction have been reported. The back propagation neural network [30] model is simple. In this approach, ocean scenes and ship motion attitudes are used as inputs and outputs. However, the prediction accuracy of this model is low. Although the radial basis function neural network [31] has good generalizability and a high learning speed, its prediction accuracy is still unsatisfactory. In fact, the three-axis rotation parameters of ships are closely related to sea conditions, which are closely related to the micro-Doppler frequency of ships. To verify the feasibility of using time-varying data with micro-Doppler frequencies to predict ship rotation and avoid the drawback of low parameter estimation accuracy, an LSTM neural network model [32] is constructed in this paper to study the prediction of ship three-axis rotation parameters based on the micro-Doppler frequencies. The LSTM neural network can process long time series data and has a long-term memory function. Therefore, the LSTM neural network is used to establish a mapping relationship between the coefficients of the micro-Doppler frequency basis function and the sequence of the ship three-axis rotation parameters to estimate the ship rotation parameters.

The LSTM neural network is a time recursive network that fundamentally addresses the gradient disappearance and long-term dependence problems in recurrent neural networks [33]. It can store historical data and flexibly adapt to specified learning tasks. The memory unit of the LSTM neural network consists of an input gate, an output gate, and a forget gate. These values correspond to the writing, reading, and resetting of the previous state of the basis function coefficient matrix, respectively [34]. The unit structure of LSTM is shown in Fig. 2. x_t is the input data of the neural network, Ξ is the activation function of the LSTM gate, and the sigmoid function is used to limit the output of the gate to achieve the retention and forgetting of information. $\tan h$ is the activation function for the processing data that enhances the capability of the data model. h_{t-1} is the hidden layer value of the previous time, c_{t-1} is the cell state value of the previous time, i_t is the control vector of the input gate at time t, $\tilde{C}_t$ is the input information vector at time t, h_t is the hidden layer value at time t, y_t is the output value at the current time, and c_t is the cell state value at the current time [35].

In the LSTM unit structure diagram mentioned above, the forget gate structure is composed of a sigmoid function and a dot product function. The sigmoid function is represented by Ξ and is given by the following [35], [36], [37]:

$$S(x_t) = \frac{1}{1 + e^{-x_t}}. \tag{20}$$

In the forget gate, the degree of forgetting at the previous moment is expressed as f_t, and is given by the following:

$$f_t = \Xi\left(Q_f \cdot [h_{t-1}, x_t] + b_f\right) \tag{21}$$

where Q_f is the weight function of the forget gate and b_f is the forget gate bias.

In the input gate, the output results i_t of the input gate can be represented as follows:

$$i_t = \Xi\left(Q_i \cdot [h_{t-1}, x_t] + b_i\right) \tag{22}$$

where Q_i is the weight function of the input layer and b_i is the input layer bias.

After adding new inputs, it is necessary to update the status of the previous moment. i_t of the input gate is multiplied by the input information vector. Then, it is added to the state vector of the previous time to obtain the state value of the current time according to the following:

$$c_t = f_t * c_{t-1} + i_t * \tilde{C}_t. \tag{23}$$

The result of the output gate represents the degree to which the current state has been filtered, and the output result can be expressed as follows:

$$O_t = \Xi\left(Q_o \cdot [h_{t-1}, x_t] + b_o\right) \tag{24}$$

$$h_t = O_t * \tanh c_t \tag{25}$$

$$y_t = h_t \tag{26}$$

where Q_o is the weight function of the output gate and b_o is the output layer bias.

By using the above formula, the input gate introduces information, and the output gate filters the state, improving the memory ability for longer time series. The process of constructing the LSTM neural network prediction model mainly includes loading and preprocessing the data, setting the LSTM model parameters, training the LSTM model, and evaluating the prediction results.

The LSTM model structure designed in this article is shown in Fig. 3. The model consists of two LSTM layers and one dense layer. The neural network input layer $x = \{x_1, x_2, \ldots, x_t\}$ is used to input micro-Doppler frequencies with t sampling points, the coefficients $W_{j1}, W_{j2}, \ldots, W_{jL_B}$ of the basis function, and the significant scatterer coordinates $r_{sj}, a_{sj}, h_{sj}, j = 1, 2 \ldots, P'$, where

$$x_i = \begin{bmatrix} f_{d,1}(i) & f_{d,2}(i) & \ldots & f_{d,P'}(i) \\ W_{11} & W_{21} & \ldots & W_{P'1} \\ W_{12} & W_{22} & & W_{P'2} \\ \vdots & & & \\ W_{1L_B} & W_{2L_B} & \ldots & W_{P'L_B} \\ r_{s1} & r_{s2} & \ldots & r_{sP'} \\ a_{s1} & a_{s2} & \ldots & a_{sP'} \\ h_{s1} & h_{s2} & \ldots & h_{sP'} \end{bmatrix}.$$

Then, the LSTM layer can be used for feature extraction from

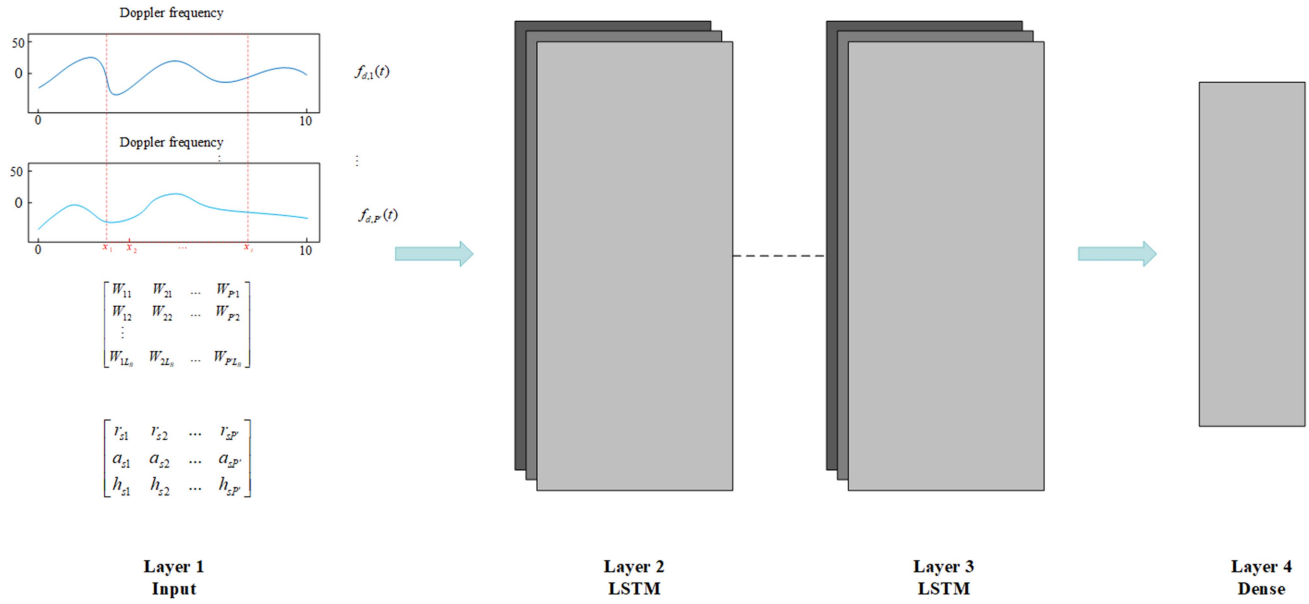

Fig. 3. LSTM network model for inverting the three-axis rotation parameters of a ship.

the matrix. To improve the model's generalization ability, we added a dropout mechanism between the LSTM layer and the dense layer. The dropout mechanism prevents overfitting of the model through partial connections. Finally, the output layer of the neural network is used to output the three-axis rotation parameters $y_t = [A_r, T_r, \varphi_r, A_r', T_r', \varphi_r', A_r'', T_r'', \varphi_r'', A_p, T_p, \varphi_p, A_p', T_p', \varphi_p', A_p'', T_p'', \varphi_p'', A_y, T_y, \varphi_y, A_y', T_y', \varphi_y', A_y'', T_y'', \varphi_y'']$ of the ship.

To facilitate analysis and avoid the influence of different dimensions of the data on the training of neural network models, it is necessary to normalize all data. The coefficient matrix in the generalized linear regression model of the input data and the three-axis rotation parameters of the output data are limited to [0,1]. The normalization expression used in this article is as follows:

$$X' = \frac{X - M_{\min}}{M_{\max} - M_{\min}} \tag{27}$$

where X is the actual value of the sample, X' is the normalized value of the sample, $M_{\max}$ is the maximum value in the neural network training dataset, and $M_{\min}$ is the minimum value in the neural network training dataset.

After the input and output data are normalized, it is necessary to set the parameters of the neural network, which mainly include the input feature dimension, number of neuron nodes, number of hidden layers, learning efficiency, and number of iteration rounds. The parameter settings affect the efficiency and accuracy of the training results. Moreover, to prevent overfitting in the neural network, it is necessary to select appropriate network parameters to ensure high-precision estimation of the three-axis rotation parameters of the ship.

The dataset consisting of the coefficient matrices and rotation parameters was trained and predicted after data preprocessing and model parameter configuration. The prediction results were analyzed using the mean square error after denormalizing the predicted data. The mean square error is the estimation error of the overall data, and is given by the following:

$$\mathrm{RMSE} = \sqrt{\frac{1}{N_s}\sum_{ii=1}^{N_s}(\mathrm{obs} - \mathrm{pre})^2} \tag{28}$$

where N_s is the dimension of the predicted data, obs is the theoretical value of the three-axis rotation parameter, and pre is the predicted value of the three-axis rotation parameter.

C. 3-D Coordinate Inversion Method for Ship Scatterers Based on an LSTM Neural Network

When ships undergo 3-DOF motion, as they simultaneously rotate along all the three axes, the direction and speed of rotation of the rotation axis vary with time. Consequently, the Doppler frequency of the scatterers also varies with time. This time-varying Doppler frequency can be used to obtain information regarding the 3-D coordinates of the scatterers. To achieve 3-D reconstruction of moving ship targets, it is essential to fully exploit the ship's 3-DOF micro-Doppler frequency and three-axis rotation parameters.

Multiple scatterers corresponding to the same ship share the same three-axis rotational angular velocity parameters. The three-axis rotation parameters of the ships are calculated as described in Section III-B. Due to the complex nonlinear relationship between the micro-Doppler frequency of the ship scatterers and the 3-D coordinates, the three-axis rotation parameters of the ships, and the 3-D coordinates of the antenna phase centers, it is difficult to directly apply traditional methods to solve the 3-D coordinate inversion optimization model of the ship scatterers. Therefore, similar to the approach of solving ship rotation parameters in Section III-B by using neural networks, we transform the nonlinear function-solving problem of the

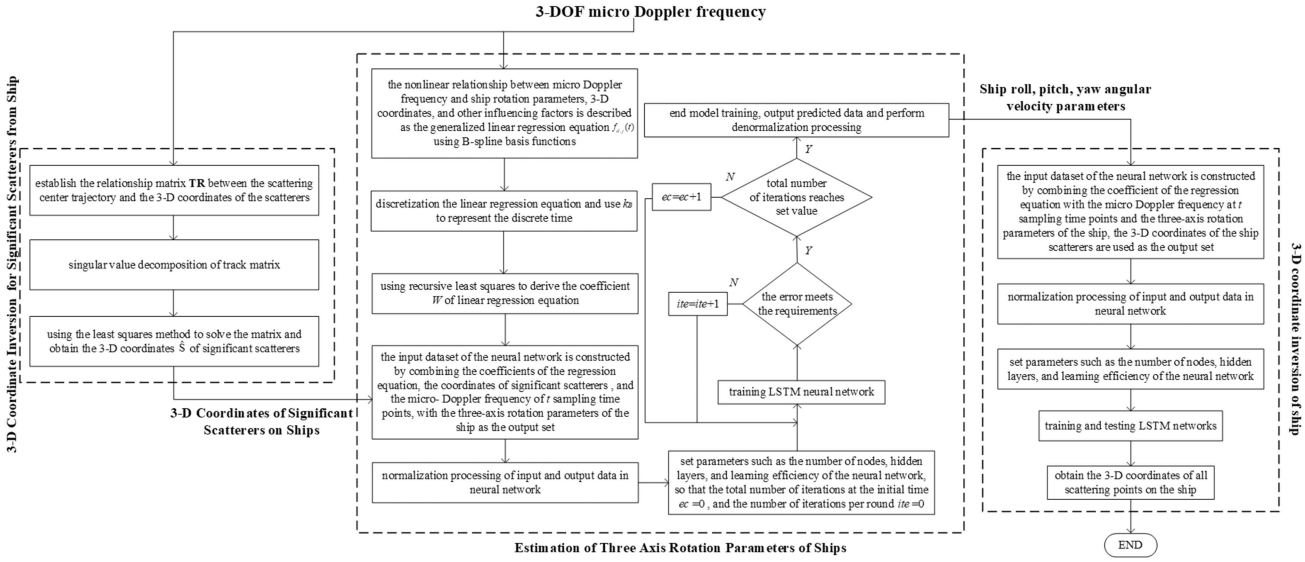

Fig. 4. Processing flow of the proposed algorithm.

ship scatterer 3-D coordinate inversion optimization model into a generalized linear regression problem, for which we utilize basis functions to solve the linear regression equation. First, we construct the generalized linear regression equation using B-spline basis functions as described in Section III-B-1). Based on the ship scatterer micro-Doppler frequency, we solve for the coefficients of the regression model using recursive least squares. Then, we build an LSTM neural network, as shown in Fig. 3. Then, an LSTM neural network is constructed, as shown in Fig. 3. The input layer is used to input the micro-Doppler frequencies with t sampling time points, regression model coefficients $W_{j1}, W_{j2}, \ldots, W_{jL_B}$, measured values of the antenna phase center X_r, Y_r, Z_r, and estimated values of the rotation parameters of the ship, including A_r, T_r, φ_r, A_r', $T_r{}'$, $\varphi_r{}'$, A_r'', T_r'', φ_r'', A_p, T_p, φ_p, A_p', $T_p{}'$, $\varphi_p{}'$, A_p'', T_p'', φ_p'', A_y, T_y, φ_y, A_y', $T_y{}'$, $\varphi_y{}'$, A_y'', T_y'', φ_y''. The output layer of the neural network provides the estimated values of r_{sj}, a_{sj}, h_{sj}.

According to the neural network processing process in Section III-B2, first, the input and output data are normalized, and then, the neural network parameters such as the number of neuron nodes, number of hidden layers, learning efficiency, and number of iteration rounds are set. After completing the data preprocessing and parameter setting steps, the dataset was trained and predicted. Finally, after the prediction data are denormalized, the root-mean-square deviation described in (28) is used to analyze the prediction results.

The main processing flow of the algorithm is shown in Fig. 4. The input of the algorithm is the 3-DOF micro-Doppler frequency of the ship described in [12]. First, the 3-DOF micro-Doppler frequency is used to establish the instantaneous distance change matrix between the scattering center and the antenna phase center, and the scatterers are correlated to establish the relationship between the scattering center trajectory matrix and the 3-D coordinates of the significant scatterers. The singular value decomposition method described in Section III-A is used to decompose the track matrix. Subsequently, the least squares method is used to determine the 3-D coordinates $\hat{S}$ of the significant scatterers.

After obtaining the 3-D coordinates of the significant scatterers of the ship, the relationships between the 3-DOF micro-Doppler frequency of the scatterers and their many influencing factors (ship three-axis rotation parameters, scatterer 3-D coordinates, azimuth time, oblique range coordinates, azimuth coordinates, and elevation coordinates) are established, and a mathematical model of the ship's three-axis rotation parameters is established. Using the B-spline basis function as described in Section III-B, the optimization model of multivariate nonlinear rotational parameters is transformed into the generalized linear regression equation $f_{d,j}(t)$. Then, the recursive least squares method is used to derive the coefficient W_{jL_B} of the basis function corresponding to j significant scatterers, and the derived coefficient matrix is combined with the 3-D coordinates of the significant scatterers obtained in Section III-A, as well as the micro-Doppler frequencies of t sampling time points, to construct a dataset for the neural network.

The obtained dataset is used as the input set of the neural network, and the three-axis rotation parameters of the ship are used as the output set of the network. The normalization method described in Section III-B is used to preprocess the input and output data, limiting the data to between [0, 1]. Then, the model parameters of the neural network are set. The parameters of the LSTM network, such as the number of nodes, hidden layers, learning rate, number of training iteration rounds, training batch, and the input and output layers, are set. The number of training iteration rounds is $\mathrm{ec} = 0$ at the initial time. The number of iteration rounds is $\mathrm{ite} = 0$ at the initial time. A neural network training model is built, and the training data are obtained. The gradient error of each training round is evaluated to examine if it meets the requirements until all iteration rounds are processed.

When the training of the LSTM neural network is complete, the network is used to process the test set data, and the output results of the test set are subjected to reverse normalization. The

TABLE I
MAIN PARAMETERS USED IN THE UNMANNED SHIP EXPERIMENT PROCESS

Parameter	Value	Parameter	Value
Carrier frequency	77 GHz	Bandwidth	3.78 GHz
PRF	1000 Hz	Accumulation time	10 s
Number of sampling points in the azimuth direction	10000	Number of sampling points in the range direction	862
Translational speed of unmanned ship	2 m/s	Distance between the radar and ships	20 m

mean square error analysis is used to predict the results and obtain the 3-DOF rotation parameters of all ships. Similarly, an inversion optimization model is established for the 3-D coordinates of ship scatterers using the three-axis rotation parameters of the ship, the coefficients of the basis function, the slant range coordinates of the scatterers as the input matrix of the LSTM network, and the 3-D coordinates of the ship as the output matrix of the LSTM network to train the network. The test set data were processed using a network to obtain the 3-D coordinates of all ship scatterers.

IV. SIMULATION EXPERIMENTS AND RESULTS ANALYSIS

A. Analysis of the Results of Fitting the Angular Velocity Curve With the Three Cosine Functions

To verify the effectiveness of the proposed three-cosine function in describing the three-axis rotational angular velocity of ships, this paper uses both the three-cosine function and the traditional cosine function to fit the measured data of the three-axis rotational angular velocity of unmanned ships. Table I shows the main parameters used in the unmanned ship experiment, and Fig. 5 shows the fitting results. Fig. 5(a), (c), and (e) show the roll, pitch, and yaw angular velocities fitted with a single cosine function, respectively. Fig. 5(b), (d), and (f) show the roll, pitch, and yaw angular velocities fitted with a three-cosine function, respectively. It is observed that the three-cosine functions provide a significantly more accurate description of the variation pattern of the three-axis rotation.

B. Integrated Motion Compensation and Micro-Doppler Frequency Extraction Results

The definition of the 3-DOF micro-Doppler frequency of ship scatterers in this article refers to the Doppler frequency caused by the three-axis rotation of the ship when both the motion of the radar platform and the translational motion of the ship are compensated. Therefore, the first step is to perform motion compensation for the radar platform and the target. This article uses the parameters shown in Table II for these calculations. First, the motion of the radar platform is compensated using the range migration correction method in the SAR RD algorithm. Then, combined with the ISAR translation compensation method, the ship target translation is compensated. The compensated echo signal is extracted using the method reported in [12] for micro-Doppler

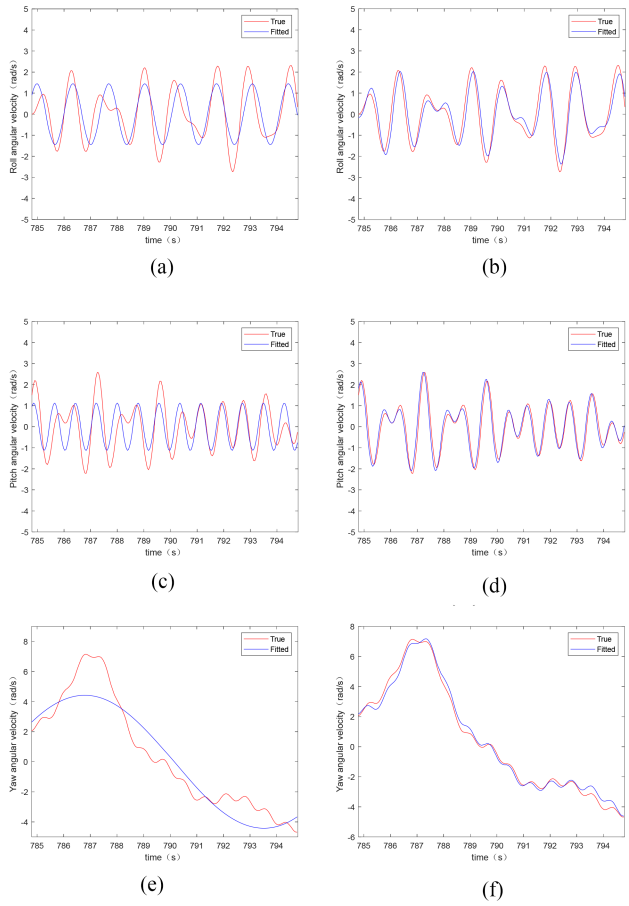

Fig. 5. Fitting results of the three-axis rotational angular velocity for unmanned ships. (a) Fitting results of the single cosine function roll angular velocity. (b) Three-cosine sum function roll angular velocity fitting results. (c) Fitting results of the single-cosine function pitch angular velocity. (d) Three-cosine sum function pitch angular velocity fitting results. (e) Fitting results of the single-cosine function yaw angular velocity. (f) Three-cosine sum function yaw angular velocity fitting results.

TABLE II
MAIN PARAMETERS OF SIMULATION EXPERIMENTS

Parameter	Value	Parameter	Value
Radar platform speed	50 m/s	Synthetic aperture time	10 s
Ship translation speed	10 m/s	Platform altitude	5 km
Carrier frequency	5.4 GHz	PRF	500 Hz
Randomly selected scatterer 1 coordinates	(-52, -4,0)	Randomly selected scatterer 2 coordinates	(7,20,0)

frequency extraction. Fig. 6 shows the simulation results of the above process. Fig. 6(a) shows the compressed distance of the echo signal from two randomly selected scatterers, Fig. 6(b) shows the compensated motion of the SAR platform, Fig. 6(c) shows the compensated target translational motion, and Fig. 6(d) shows the extracted micro-Doppler frequency. It is observed from Fig. 6 that the micro-Doppler frequency extraction results

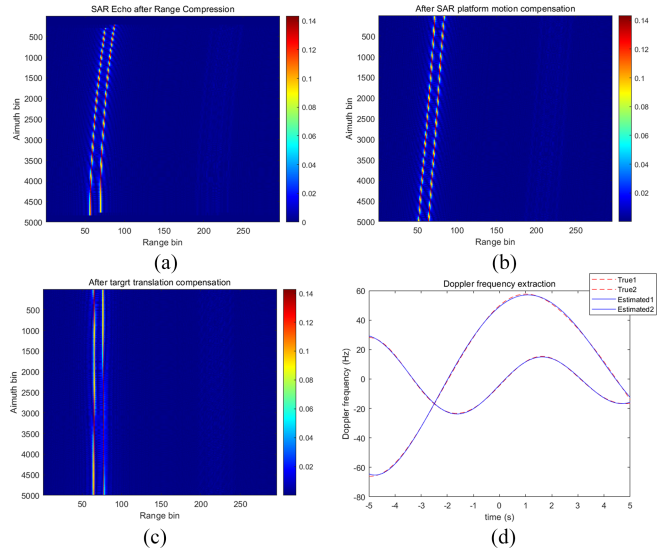

Fig. 6. SAR platform motion and target motion compensation and micro-doppler frequency extraction results. (a) Two scatterers are randomly selected, and the distance of the echo signal is reduced to obtain the result. (b) Results of compensating for the motion of the SAR platform. (c) Results of compensating for target translational motion. (d) Scatterers' micro-doppler frequency extraction results.

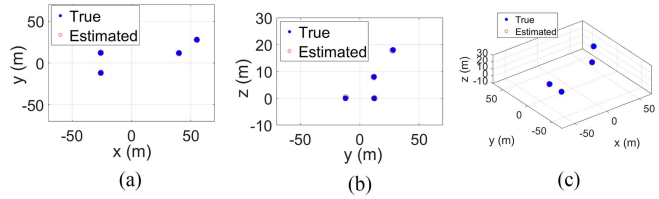

Fig. 7. 3-D coordinate inversion results for significant scatterers. (a) Top view. (b) Side view. (c) 3-D view.

are very close to the true values, with a root mean square error of 0.41 Hz.

C. 3-D Coordinate Inversion Results for Significant Scatterers

This article continues to use the parameters listed in Table II for significant scatterer inversion. Fig. 7 shows the simulation results of the 3-D coordinate inversion of significant scatterers obtained using the method proposed in Section III-A, including the top view, side view, and 3-D view. It is observed from the figure that the 3-D coordinates of the inverted scatterers are very close to the true values. Statistical analysis shows that the average deviation of the inverted scatterer coordinates is less than 0.5 m. The inversion results are shown in Table III.

D. Estimation Results of Ship Three-Axis Rotation Parameters

To verify the effectiveness of the proposed method for estimating the three-axis rotation parameters of time-varying ships, simulated data processing was carried out. First, a 3-D model of a ship with 70 scatterers is established. Except for the coordinates of the scatterers, the settings of the other parameters are the same as those in Table II. Using the above simulation parameters and utilizing the simulation theory of ship roll, pitch, and yaw motion

TABLE III
SIGNIFICANT SCATTERERS' COORDINATE INVERSION ERROR

Scatterer Number	True Coordinates	Inversion Coordinates	Average Error
1	(-26,12,0)	(-25.59,12.29,0.31)	0.34 m
2	(-26, -12,0)	(-26.12, -12.05, -0.44)	0.20 m
3	(40,12,8)	(40.2,12.07,8.09)	0.12 m
4	(55,28,18)	(55.14,28.39,18.17)	0.23 m

under different wave effects, a total of 80 000 sets of data on the three-axis rotational angular velocity of ships under five sea conditions are constructed. The angular velocity of this dataset is used in the micro-Doppler frequency extraction formula in [12] to obtain the instantaneous Doppler frequency dataset corresponding to the scatterers under different sea conditions. Then, the significant scatterer estimation method proposed in Section III-A and the coefficient matrix recursive formula in Section III-B are used to obtain the significant scatterers and coefficient matrix dataset. In this section, the number of hidden layers in the LSTM network is set to 2, the number of neuron nodes is set to 32, the learning rate is set to 0.0001, and the number of iterations is set to 10 000. The instantaneous Doppler frequency dataset, significant scatterer coordinate dataset, and coefficient matrix dataset are used as inputs for the neural network, the angular velocity dataset is used as the true values of the rotation parameters and the output values of the neural network training set, and the mean square error is calculated. The sample dataset was divided into training and testing sets, 80% of the samples were randomly selected for model training, and the remaining 20% were selected for validation.

Two types of ship rotation parameters are randomly selected for simulation analysis under sea conditions, and Fig. 8 shows the relevant processing results. Fig. 8(a) and (b) show the estimated values of the time-varying roll angle velocity of ships under two sea conditions obtained using the method proposed in this article. To facilitate the analysis of the accuracy of the estimation results, the true values of the ship's rotational angular velocity are also shown in Fig. 8(a) and (b). Good agreement between the estimated and true values of the ship roll angular velocity is observed. Statistical analysis shows that the mean square deviations of the estimated roll angular velocity values for the data presented in Fig. 8(a) and (b) are approximately 0.32°/s and 0.47°/s, respectively.

Fig. 8(c) and (d) show the estimated values of the pitch angular velocity of the ship under two sea conditions obtained using the method proposed in this article. To facilitate the qualitative evaluation of the accuracy of the estimated values, the true value curves of the pitch angular velocity are also shown in Fig. 8(c) and (d). The accuracy of the estimation of the pitch angular velocity is relatively high under both sea conditions. Statistical analysis shows that the mean square deviations of the estimated pitch rotational angular velocity values for the data presented in Fig. 8(c) and (d) are approximately 0.27°/s and 0.42°/s, respectively.

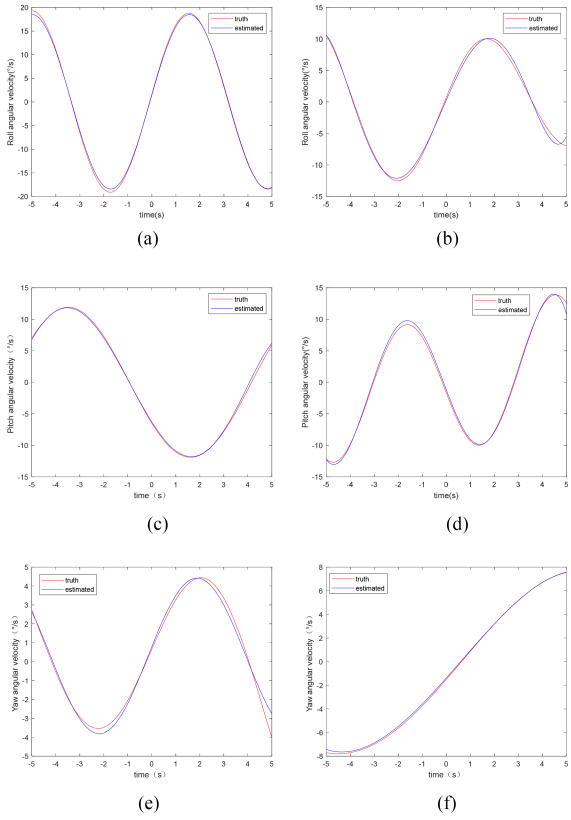

Fig. 8. Simulation results of the ship three-axis rotational angular velocity curve. (a) Ship roll angular velocity curve for the first sea state. (b) Ship roll angular velocity curve for the second sea state. (c) Ship pitch angular velocity curve for the first sea state. (d) Ship pitch angular velocity curve for the second sea state. (e) Ship yaw angular velocity curve for the first sea state. (f) Ship yaw angular velocity curve for the second sea state.

Fig. 8(e) and (f) show the estimated values of the ship yaw rate under two sea conditions obtained using the method proposed in this article. As in the previous subfigures, the true value curves of the ship yaw angles are also shown in Fig. 8(e) and (f). An examination of Fig. 8(e) and (f) reveals good agreement between the estimated and true values of the ship yaw rate. Statistical analysis shows that the mean square deviations of the estimated yaw angular velocity for the data presented in Fig. 8(e) and (f) are approximately 0.28°/s and 0.12°/s, respectively. The analysis in Fig. 8 shows that the proposed method achieves high estimation accuracy and has important application value in estimating the roll, pitch, and yaw parameters of ships.

E. Inversion Results of Ship's 3-D Coordinates

To confirm the effectiveness of the proposed method in inferring the 3-D coordinates of ships, we continued processing the simulated data. Additionally, we compared the proposed method with the SAR Doppler parameter estimation method outlined in reference [11]. Throughout the simulation process, the parameters listed in Table II were consistently applied. The ideal scattering model of all ship scatterers (a total of 70) is depicted in Fig. 9(a) to (d).

The 3-D reconstruction method outlined in [11] involves coordinate calculations based on the rotational motion of the target and exhibits varying performance under different rotation scenarios. In this article, simulations were conducted under the condition of a ship undergoing three-axis rotation. Fig. 10(a) and (b) depict the 3-D coordinate reconstruction results obtained using this method. A comparison with Fig. 9(a) to (d) reveals significant discrepancies between the inferred 3-D positions and the model positions. Through statistical analysis, the maximum error was found to be 15.7 m with an average difference of 10.4 m between the coordinates of the 70 inverted scatterers and their true coordinates.

Using the dataset constructed in Section IV-D, a new LSTM neural network is trained. The instantaneous Doppler frequency dataset, coefficient matrix dataset, and angular velocity dataset are used as inputs to the neural network, while the ship's 3-D

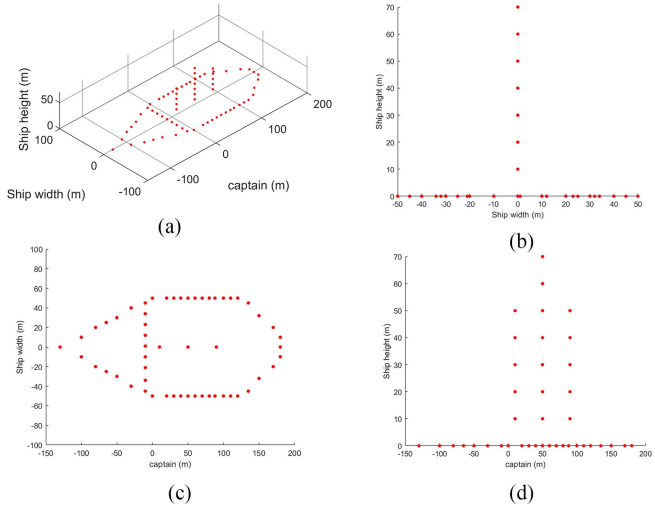

Fig. 9. 3-D coordinate model of ship scatterers. (a) Schematic diagram of the 3-D model of the ship target. (b) Schematic diagram of ship projection on the *YOZ* plane. (c) Schematic diagram of ship projection on the *XOY* plane. (d) Schematic diagram of ship projection on the *XOZ* plane.

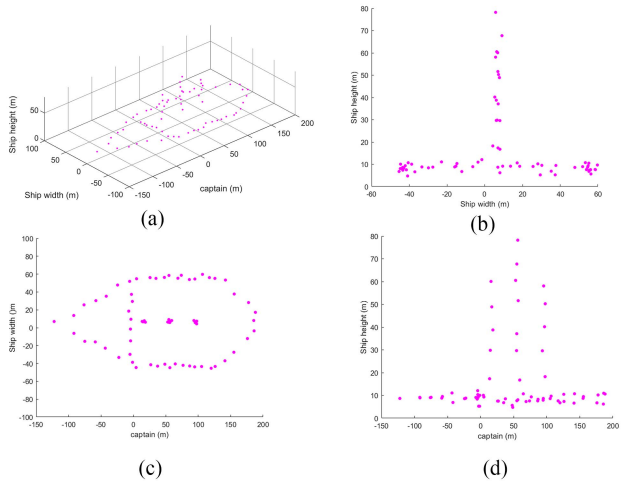

Fig. 10. 3-D coordinates of the ship scatterers were obtained through the method outlined in [11]. (a) Inversion results of the ship 3-D model. (b) Projection of the ship inversion model on the *YOZ* plane. (c) Projection of the ship inversion model on the *XOY* plane. (d) Projection of the ship inversion model on the *XOZ* plane.

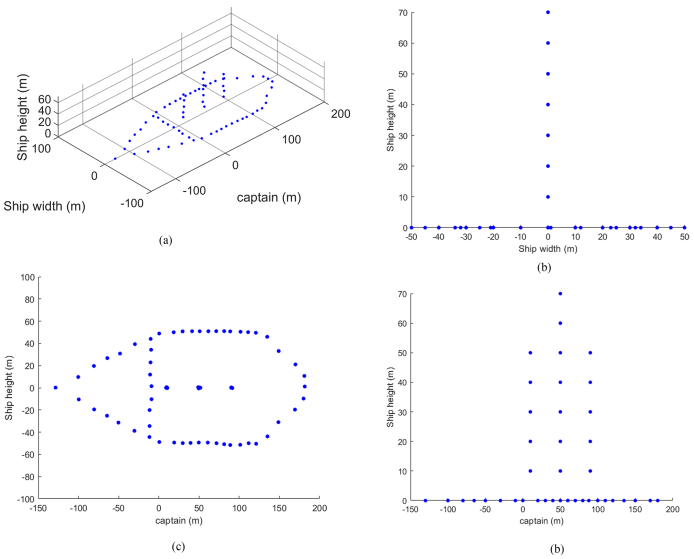

Fig. 11. Inversion results of the 3-D coordinates of the ship scatterers. (a) Inversion results of the ship 3-D model. (b) Projection of the ship inversion model on the *YOZ* plane. (c) Projection of the ship inversion model on the *XOY* plane. (d) Projection of the ship inversion model on the *XOZ* plane.

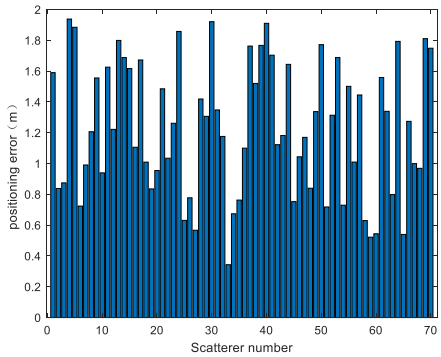

Fig. 12. Inversion error of 3-D coordinates of ship scatterers.

coordinate dataset provides the output values for the training set. The dataset is split into training and testing sets, with 80% of the samples randomly selected for training the model and the remaining 20% for validation. The neural network parameters are set as follows: two hidden layers, each with 32 neuron nodes, a learning rate of 0.0001, and 10 000 iterations.

Upon estimating the ship's three-axis rotational angular velocities, the newly constructed network is used to invert the ship's 3-D coordinates. Fig. 11(a)–(d) depict the inverted 3-D coordinates of the ship target. A comparison with Fig. 9(a)–(d) reveals that the inverted 3-D positions closely match the model positions. The results of a statistical analysis of the inversion errors for each scatterer are shown in Fig. 12, and indicate that the maximum error is consistently within 2 m. The average difference between the coordinates of the 70 inverted scatterers and their true coordinates is calculated to be 1.23 m. Consequently, it is observed that the proposed method achieves higher estimation accuracy compared to the method presented in [11].

The specific information regarding the calculations of the two algorithms is presented in Table IV. Although the algorithm

TABLE IV
EVALUATION OF ALGORITHM INVERSION RESULTS

Algorithm	Maximum Error	Average Error	Computational Load
[11]	15.75 m	10.4 m	26.8 s
Proposed algorithm	1.93 m	1.23 m	107.6 s

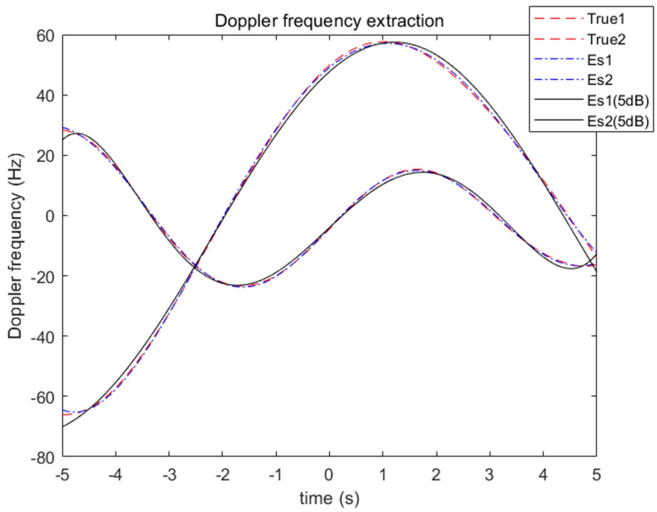

Fig. 13. Extraction results of the micro-doppler frequency for scatterers with an SNR of 5 dB.

proposed in this paper is more time-consuming, both the average inversion error and the maximum inversion error of the scatterers are significantly smaller than those of the algorithm in [11]. This validates the effectiveness of the algorithm proposed in this article.

F. Algorithmic Robustness

Due to the influence of noise on the extraction of target echo Doppler frequencies, the estimation of three-axis rotation parameters of ships and the reconstruction of the 3-D coordinates of scatterers are affected. To verify the performance of the algorithm in a noisy environment, Gaussian white noise is added to the echo signal model, while the ship's scatterer model and other parameters remain unchanged. The results of the extraction of the Doppler frequency of two scatterers under a signal-to-noise ratio (SNR) of 5 dB are shown in Fig. 13. The true values of the Doppler frequency are represented by the red curve, while the blue curve represents the Doppler frequency extracted by the method in [12] without noise, and the black curve represents the Doppler frequency extracted by the method in [12] with an SNR of 5 dB. The extraction accuracy of the Doppler frequency is minimally affected by noise, with a root mean square error (RMSE) of 1.4 Hz. Therefore, the method proposed in this paper still demonstrates good robustness in the subsequent estimations of the ship's three-axis rotation parameters and inversion of 3-D coordinates using the Doppler frequency.

Using the scatterer micro-Doppler frequency extracted under an SNR of 5 dB, the estimated results for the ship's three-axis

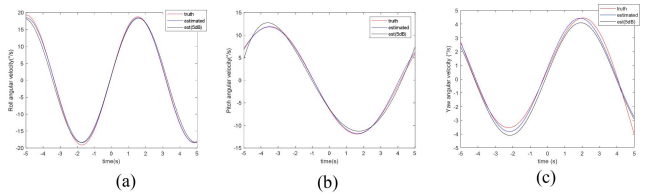

Fig. 14. Estimation results of the ship's three-axis rotational angular velocity at an SNR of 5 dB. (a) Ship roll angular velocity at an SNR of 5 dB. (b) Ship pitch angular velocity at an SNR of 5 dB. (c) Ship yaw angular velocity at an SNR of 5 dB.

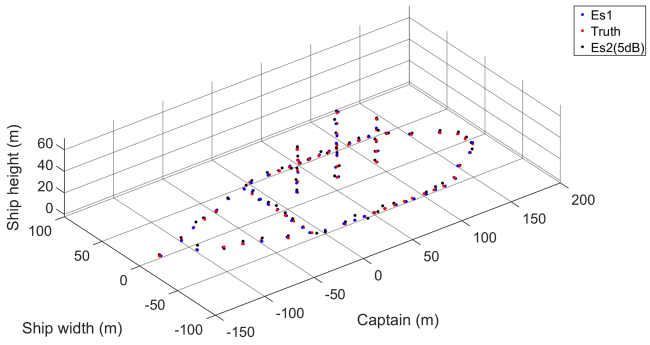

Fig. 15. Inversion results of the ship's 3-D coordinates at an SNR of 5 dB.

rotation parameters obtained using the method proposed in this paper are shown in Fig. 14. The red curve represents the true values of the ship's angular velocities, the blue curve represents the estimated angular velocities of the ship's rotation without noise using the method proposed in this article, and the black curve represents the estimated angular velocities of the ship's rotation using the method proposed in this article with an SNR of 5 dB. The RMSEs of the estimated roll, pitch, and yaw angular velocities corresponding to Fig. 14(a)–(c) are approximately 0.91°/s, 0.62°/s, and 0.41°/s, respectively.

Using the scatterer micro-Doppler frequency and the estimated three-axis rotation parameters of the ship extracted under an SNR of 5 dB, the 3-D imaging results of the ship obtained using the method proposed in this article are shown in Fig. 15. The red dots represent the true 3-D coordinates of the ship, the blue dots represent the 3-D coordinates of the ship inverted by the method proposed in this paper without noise, and the black dots represent the 3-D coordinates of the ship inverted by the method proposed in this paper with an SNR of 5 dB. It can be observed that the maximum error is controlled within 5 m, and the average distance difference between the calculated coordinates of the 70 inverted scatterers and the true coordinates is 2.49 m.

Under the 5 dB noise condition, the algorithm can still accurately obtain the 3-D coordinate information of the target scatterers. Eighteen Monte Carlo simulation experiments were conducted under different SNR conditions, and the values of the average distance difference between the reconstructed 3-D coordinates of the scatterers and the true coordinates for different SNR values are shown in Table V. As the SNR decreases, the coordinate reconstruction error gradually increases. When the SNR is lower than –5 dB, the reconstruction average error exceeds 5 m. Therefore, the algorithm proposed in this article can achieve good 3-D ship imaging when the SNR is higher than –5 dB.

TABLE V
MEAN ERRORS OF 3-D COORDINATE INVERSION FOR SHIPS WITH DIFFERENT SNRS

SNR	10 dB	9 dB	8 dB	7 dB	6 dB	5 dB
Distance error	1.44 m	1.54 m	1.73 m	1.89 m	2.16 m	2.39 m
SNR	4 dB	3 dB	2 dB	1 dB	0 dB	-1 dB
Distance error	2.75 m	2.94 m	3.24 m	3.38 m	3.67 m	3.94 m
SNR	-2 dB	-3 dB	-4 dB	-5 dB	-6 dB	-7 dB
Distance error	4.23 m	4.59 m	4.88 m	5.12 m	5.47 m	5.72 m

V. REAL DATA VALIDATION AND RESULTS ANALYSIS

A. Estimation Results of Ship Three-Axis Rotation Parameters

Due to the difficulty of simulating the impact of real environments on ships and radar systems in simulation experiments, unmanned ship measurement experiments were conducted to comprehensively test the performance of the proposed method in real environments.

In this article, we utilize an intelligent car radar system platform and an unmanned ship built in the actual experiment of [12] to collect the measured echo data of unmanned ships in a certain sea area and verify the effectiveness of the proposed method in practical environments. A photograph of the radar system of the smart car is shown in Fig. 16(a). Fig. 16(b) shows a photograph of the tested unmanned ship, Fig. 16(c) shows a photograph taken during the detection of the ship by the radar system at a certain time, and Fig. 16(d) shows a photograph of the HWT901B-485 attitude meter that records the three-axis rotation parameters of the unmanned ship. The attitude instrument provides the true values of the roll, pitch, and yaw angular velocities for the unmanned ship experiments. The HWT901B-485 attitude sensor is equipped with a 10-axis sensor, an RM3100 module, an accelerometer, and a high-precision gyroscope. An attitude meter, which consists of microprocessors, can be used to conduct dynamic calculations. Moreover, Kalman dynamic filtering algorithms can be used to quickly process ship data, thereby solving for the real-time three-axis rotational attitude of a ship. The attitude instrument must be used to perform initialization steps such as controlling the magnetic field calibration through the supporting upper computer. After each collection is completed, the collected attitude data are transmitted to the workstation, and then data processing is carried out on the workstation using

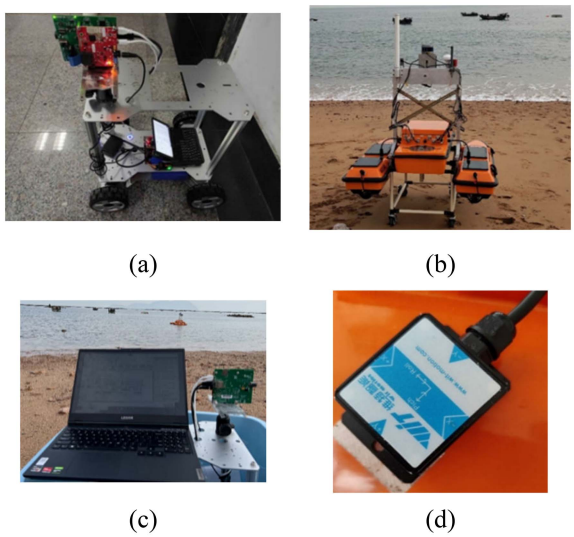

Fig. 16. Radar system and test scenario. (a) Photograph of the radar system installed on an intelligent car. (b) Photograph taken when the unmanned ship is stationary. (c) Photograph taken during radar detection of an unmanned ship. (d) Photograph of the HWT901B-485 attitude sensor.

software written in MATLAB. The composition, usage method, and data transmission method of the radar system constructed in this experiment are consistent with those of the turntable experiment described in [12, Section IV-B].

Table I in Section IV of this article lists the main parameters used during the experimental process. After distance compression and translation compensation were performed on the obtained unmanned ship echo data, the instantaneous Doppler frequency was estimated using the method in [12], and the roll, pitch, and yaw three-axis rotational angular velocities of the unmanned ship were subsequently estimated using the method described in Section III-B. Fig. 17 shows the relevant experimental results. Fig. 17(a) and (b) show the estimated roll angular velocities of the ship during different periods after processing using the method presented in this paper. Fig. 17(a)–(f) show the angular velocity of the ship at different periods after processing using the estimation method proposed in this article. The red curve displays the true value of the ship's rotational angular velocity obtained from the attitude sensor. Statistical analysis reveals that the mean squared deviations of the estimated roll angular velocity values presented in Fig. 17(a) and (b) are approximately 0.31°/s and 0.11°/s, respectively. Fig. 17(c) and (d) show the pitch angular velocity of the ship at different periods after processing using the estimation method presented in this article. Statistical analysis reveals that the mean square deviations of the estimated pitch angular velocity values presented in Fig. 17(c) and (d) are approximately 0.24°/s and 0.26°/s, respectively. Fig. 17(e) and (f) show the yaw angular velocity of the ship at different periods after processing using the estimation method presented in this article. Statistical analysis reveals that the mean square deviations of the estimated yaw rate values presented in Fig. 17(e) and (f) are approximately 0.18°/s and 0.12°/s, respectively. Analysis of the results presented in Fig. 17 shows that the method proposed in this article still has

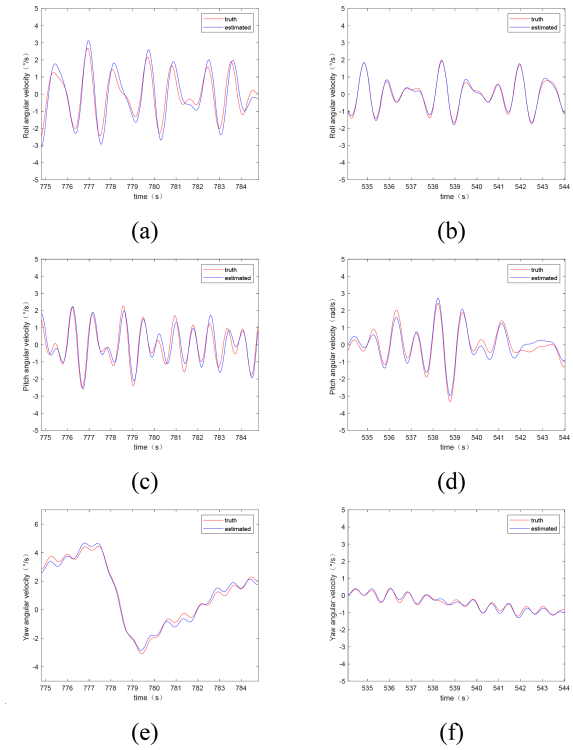

Fig. 17. Experimental results of the three-axis rotational angular velocity of unmanned ships at different times. (a) Ship roll angular velocity during the first period. (b) Ship roll angular velocity during the second period. (c) Ship pitch angular velocity during the first period. (d) Ship pitch angular velocity during the second period. (e) Ship yaw angular velocity during the first period. (f) Ship yaw angular velocity during the second period.

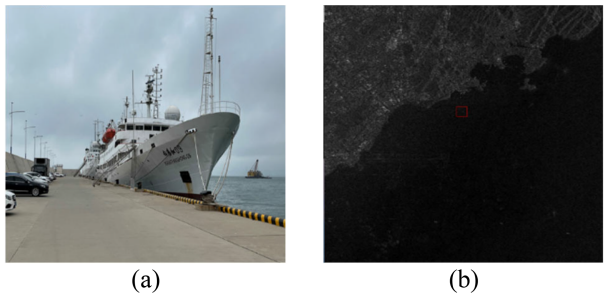

Fig. 18. Optical image and satellite data image of the ship. (a) Optical image of the Xiangyanghong-09 ship. (b) Radarsat-2 satellite data.

high estimation accuracy for the measured data, verifying the effectiveness of the method in practical environments.

To confirm the effectiveness of the proposed method, a synchronous detection experiment was conducted in a certain sea area for the Xiangyanghong-09 ship using a spaceborne SAR. During the experiment, the Xiangyanghong-09 ship maintained an average speed of 8 m/s, and synchronous transit data from the Radarsat-2 satellite were acquired for comparison. Fig. 18(a) shows an optical photograph of the Xiangyanghong-09 ship under test, while Fig. 18(b) shows the Radarsat-2 satellite data. The Xiangyanghong-09 ship is equipped with an inertial navigation system, which is a navigation parameter solving system consisting of gyros and accelerometers. This system provides

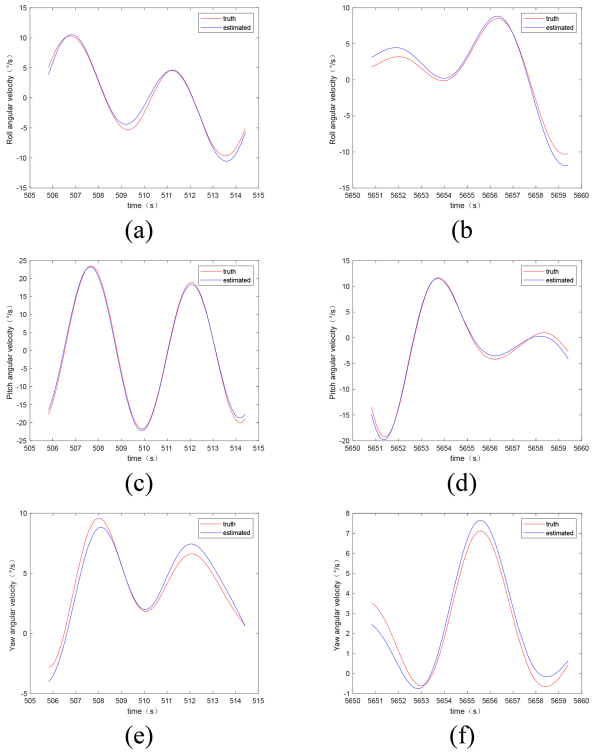

Fig. 19. Experimental results of the three-axis rotational angular velocity of the Xiangyanghong-09 ship at different times. (a) Ship roll angular velocity during the first period. (b) Ship roll angular velocity during the second period. (c) Ship pitch angular velocity during the first period. (d) Ship pitch angular velocity during the second period. (e) Ship yaw angular velocity during the first period. (f) Ship yaw angular velocity during the second period.

information such as the roll, pitch, and yaw rates of the ship. In this article, a refocusing method based on target echo positioning is used to locate and extract ship echo data based on the azimuth and range positions of ship targets in complete SAR images. Subsequently, the ship echo data are processed for SAR platform motion compensation and target translational compensation. Finally, the proposed method is applied to estimate the roll, pitch, and yaw angular velocities of the ship.

Fig. 19 shows the relevant experimental results. Fig. 19(a) and (b) show the roll angular velocities of the ship at different periods after processing using the estimation method presented in this article. Fig. 19(a) and (b) also show the true values of the ship's rotational angular velocity obtained from the attitude sensor. Statistical analysis shows that the mean square deviations of the estimated roll angular velocity values presented in Fig. 19(a) and (b) are approximately 1.57°/s and 1.78°/s, respectively. Fig. 19(c) and (d) show the pitch angular velocity of ships at different periods after processing using the estimation method presented in this article. Statistical analysis shows that the mean square deviations of the estimated pitch angular velocity values presented in Fig. 19(c) and (d) are approximately 1.37°/s and 1.86°/s, respectively. Fig. 19(e) and (f) show the yaw angular velocity of ships at different periods after processing using the estimation method presented in this paper. Statistical analysis shows that the mean square deviations of the estimated yaw angular velocity presented in Fig. 19(e) and (f) are approximately

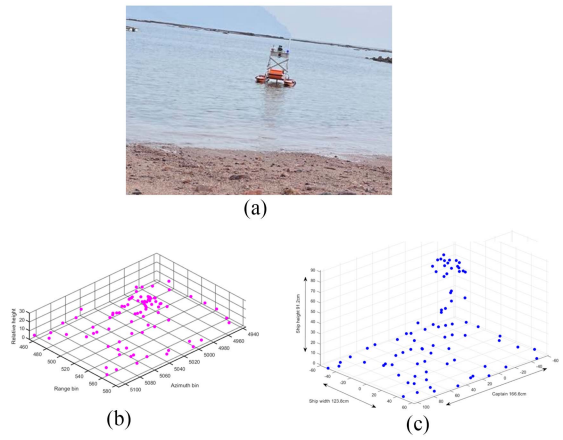

Fig. 20. Experiment on the 3-D coordinate inversion of unmanned ship. (a) Optical images of the unmanned ship. (b) 3-D coordinate inversion results of the unmanned boat using the method from [11]. (c) 3-D coordinate inversion results of the unmanned boat using the method proposed in this paper.

1.47°/s and 1.18°/s, respectively. According to the analysis in Fig. 19, the method proposed in this paper still has high estimation accuracy for the measured data of the Xiangyanghong-09 ship, further verifying the effectiveness of the method.

B. *Inversion Results of Ship's 3-D Coordinates*

In this section, we utilized the intelligent small car radar system platform and unmanned boat described in Section V-A. to collect real-measured echo data from unmanned boats in a certain sea area. We compared our method with the method proposed in [11] to verify the effectiveness of our method in actual environments. The length, width, and height of the unmanned boat shown in Fig. 20(a) are 164, 120, and 98 cm, respectively. After performing distance compression and translational compensation on the acquired echo data, we conducted 3-D coordinate inversion of the unmanned boat using both the method reported in [11] and our proposed method. The final 3-D inversion images are shown in Fig. 20.

Fig. 20(b) represents the 3-D image of the unmanned boat obtained using the method reported in [11]. Since the prior information about the rotation of the unmanned boat is unknown, the true coordinate information of the scatterers of the unmanned boat cannot be obtained. Thus, only the relative 3-D structure of the unmanned boat can be displayed.

Fig. 20(c) represents the 3-D image of the unmanned boat obtained using the algorithm proposed in this article. It is observed that the scatterers of the unmanned boat inverted by our method basically correspond to the actual target. Furthermore, the length, width, and height are generally consistent with those of the actual target. Compared to the results obtained using the method reported in [11], our method provides more realistic 3-D information about the target, demonstrating the effectiveness of the proposed method for 3-D imaging of ships.

To further validate the proposed method, synchronous transit data from the Radarsat-2 satellite, acquired during a sun-synchronous SAR detection experiment on the Xiangyanghong-09 ship, were utilized. An optical image of the

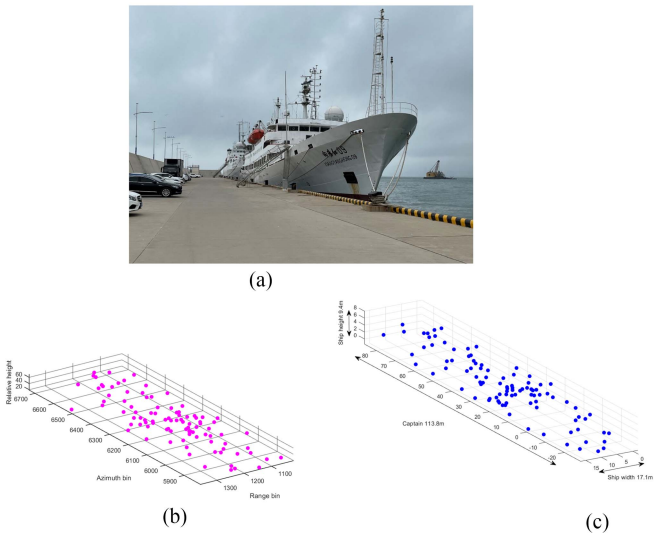

Fig. 21. 3-D coordinate inversion experiment for the Xiangyanghong-09 ship. (a) Optical image of the Xiangyanghong-09 ship. (b) 3-D coordinate inversion results of the Xiangyanghong-09 ship using the method from [11]. (c) 3-D coordinate inversion results of the Xiangyanghong-09 ship using the method proposed in this paper.

Xiangyanghong-09 ship is shown in Fig. 21(a), with measured dimensions of 112.05 m in length, 15 m in width, and 8.2 m in height. After performing distance compression, SAR platform motion compensation, and target translational compensation on the acquired ship echo data, 3-D coordinate inversion of the ship target was conducted using both the method reported in [11] and the method proposed in this article. The final 3-D inversion images are depicted in Fig. 21. Fig. 21(b) represents the 3-D image of the ship obtained using the method reported in [11]. Similar to previous cases, it is unable to solve the true coordinate information of the ship's scatterers and can only display the relative 3-D structure. Fig. 21(c) displays the 3-D image of the ship obtained using the algorithm proposed in this article. The scatterers inverted by our method basically correspond to the actual target scatterers, and the inverted dimensions are generally consistent with those of the actual target. This further demonstrates the effectiveness of the proposed method.

VI. Conclusion

High-precision inversion of the 3-D coordinates of ship scatterers is highly important for improving the imaging quality of ships and the ability to distinguish ship types. However, it is difficult to apply the existing method to this task for complex moving ship targets. To address this shortcoming, a new method for the 3-D coordinate inversion of ships based on 3-DOF micro-Doppler frequencies is proposed in this article.

In this method, after extracting the micro-Doppler frequencies from ship echo data, the 3-D coordinate inversion algorithm of the ship's significant scatterers is first studied, the change matrix of the instantaneous distance between the scattering center of the scatterer and the antenna phase center is established, and the 3-D coordinate information of several significant scatterers is estimated. Then, a multivariate nonlinear optimization model relating the scatterer micro-Doppler frequency to the 3-D coordinates of significant scatterers, the ship three-axis rotation parameters, the antenna phase center 3-D coordinates and other influencing factors is constructed. The B-spline basis function and recursive least squares method are used to solve the multivariate nonlinear optimization model to obtain the basis function and correlation coefficient matrix representing the ship scatterer micro-Doppler frequency. Then, the advantages of the LSTM network that are suitable for describing complex systems are considered. The LSTM network is used to accurately estimate the roll, pitch, and yaw three-axis rotation parameters of ships. Finally, a 3-D coordinate inversion model for ship scatterers based on the three-axis rotation parameters of the ship is established, and the LSTM network processing model is also used to achieve high-precision inversion of the 3-D coordinates of ship scatterers. The core concept of the proposed method is to accurately estimate the three-axis rotation parameters of time-varying ships, exploiting the fact that the three-axis rotation angular velocity parameters for multiple scatterers of the same ship should be the same. We have conducted multiple experiments using simulation and measured data processing to verify the high estimation accuracy of our method in multiple aspects.

Additionally, 3-D imaging of noncooperative ship targets typically occurs in extremely low-SNR environments. The method used in this study may introduce significant errors when applied to such targets. Therefore, future work will focus on introducing clutter suppression techniques to improve the accuracy of 3-D coordinate inversion for noncooperative targets.

References

[1] C. Chen, C. He, C. Hu, H. Pei, and L. Jiao, "A deep neural network based on an attention mechanism for SAR ship detection in multiscale and complex scenarios," *IEEE Access*, vol. 7, pp. 104848–104863, 2019, doi: 10.1109/ACCESS.2019.2930939.

[2] Z. Liu, Y. Jiang, Y. Wang, and Y. Du, "Radar imaging of non-stationary rotating ship target with GEO-shipborne bistatic configuration," *IEEE Sens. J.*, vol. 19, no. 13, pp. 5213–5218, Jul. 2019, doi: 10.1109/JSEN.2019.2904705.

[3] S. Shao, L. Zhang, and H. Liu, "An optimal imaging time interval selection technique for marine targets ISAR imaging based on sea dynamic prior information," *IEEE Sens. J.*, vol. 19, no. 13, pp. 4940–4953, Jul. 2019, doi: 10.1109/JSEN.2019.2903399.

[4] Y. Zhou, Z. Chen, L. Zhang, and J. Xiao, "Micro-doppler curves extraction and parameters estimation for cone-shaped target with occlusion effect," *IEEE Sens. J.*, vol. 18, no. 7, pp. 2892–2902, Apr. 2018, doi: 10.1109/JSEN.2018.2800053.

[5] I.-O. Choi, S.-H. Park, K.-B. Kang, S.-H. Lee, and K.-T. Kim, "Efficient parameter estimation for cone-shaped target based on distributed radar networks," *IEEE Sens. J.*, vol. 19, no. 21, pp. 9736–9747, Nov. 2019, doi: 10.1109/JSEN.2019.2927921.

[6] R. Cao, Y. Wang, and Y. Zhang, "Analysis of the imaging projection plane for ship target with spaceborne radar," *IEEE Trans. Geosci. Remote Sens.*, vol. 60, Apr. 2022, Art. no. 5205021, doi: 10.1109/TGRS.2021.3068690.

[7] F. Santi, M. Bucciarelli, and D. Pastina, "Target rotation motion estimation from distributed ISAR data," in *Proc. IEEE Radar Conf.*, 2012, pp. 0659–0664.

[8] F. Santi, D. Pastina, and M. Bucciarelli, "Estimation of ship dynamics with a multiplatform radar imaging system," *IEEE Trans. Aerosp. Electron. Syst.*, vol. 53, no. 6, pp. 2769–2788, Dec. 2017, doi: 10.1109/TAES.2017.2714960.

[9] T. Gu, G. Liao, Y. Li, Y. Liu, and Y. Guo, "Airborne downward-looking sparse linear array 3-D SAR imaging via 2-D adaptive iterative reweighted atomic norm minimization," *IEEE Trans. Geosci. Remote Sens.*, vol. 60, Feb. 2022, Art. no. 5202513, doi: 10.1109/TGRS.2021.3058299.
[10] T. Gu, G. Liao, Y. Li, Y. Guo, and Y. Liu, "DLSLA 3-D SAR imaging via sparse recovery through combination of nuclear norm and low-rank matrix factorization," *IEEE Trans. Geosci. Remote Sens.*, vol. 60, Aug. 2022, Art. no. 5208213, doi: 10.1109/TGRS.2021.3100715.
[11] R. Cao, Y. Wang, S. Sun, and Y. Zhang, "Three dimension airborne SAR imaging of rotational target with single antenna and performance analysis," *IEEE Trans. Geosci. Remote Sens.*, vol. 60, Mar. 2022, Art. no. 5225417, doi: 10.1109/TGRS.2022.3161051.
[12] P. Zhou, X. Zhang, Y. Dai, W. Sun, and Y. Wan, "Time window selection algorithm for ISAR ship imaging based on instantaneous doppler frequency estimations of multiple scatterers," *IEEE J. Sel. Topics Appl. Earth Observ. Remote Sens.*, vol. 12, no. 10, pp. 3799–3812, Oct. 2019, doi: 10.1109/JSTARS.2019.2943349.
[13] Y. Wang, R. Xu, Q. Zhang, and B. Zhao, "ISAR imaging of maneuvering target based on the quadratic frequency modulated signal model with time-varying amplitude," *IEEE J. Sel. Topics Appl. Earth Observ. Remote Sens.*, vol. 10, no. 3, pp. 1012–1024, Mar. 2017, doi: 10.1109/JSTARS.2016.2622721.
[14] Y. Wang and X. Chen, "3-D interferometric inverse synthetic aperture radar imaging of ship target with complex motion," *IEEE Trans. Geosci. Remote Sens.*, vol. 56, no. 7, pp. 3693–3708, Jul. 2018, doi: 10.1109/TGRS.2018.2806888.
[15] J. Zhang and Y. Wang, "A three-dimensional imaging method of ship target via multistatic distributed InISAR," *IEEE Geosci. Remote Sens. Lett.*, vol. 19, Aug. 2022, Art. no. 4511805, doi: 10.1109/LGRS.2022.3195362.
[16] X. Ai, Y. Huang, F. Zhao, J. Yang, Y. Li, and S. Xiao, "Imaging of spinning targets via narrow-band T/R-R bistatic radars," *IEEE Geosci. Remote Sens. Lett.*, vol. 10, no. 2, pp. 362–366, Mar. 2013, doi: 10.1109/LGRS.2012.2205893.
[17] X. Xu, F. Su, J. Gao, and X. Jin, "High-squint SAR imaging of maritime ship targets," *IEEE Trans. Geosci. Remote Sens.*, vol. 60, Nov. 2022, Art. no. 5200716, doi: 10.1109/TGRS.2020.3036452.
[18] B. Zhou, X. Qi, J. Zhang, and H. Zhang, "Effect of 6-DOF oscillation of ship target on SAR imaging," *Remote Sens.*, vol. 13, no. 9, May 2021, Art. no. 1821.
[19] P. Liu and Y.-Q. Jin, "A study of ship rotation effects on SAR image," *IEEE Trans. Geosci. Remote Sens.*, vol. 55, no. 6, pp. 3132–3144, Jun. 2017, doi: 10.1109/TGRS.2017.2662038.
[20] E. Masry, "Multivariate regression estimation of continuous-time processes from sampled data: Local polynomial fitting approach," *IEEE Trans. Inf. Theory*, vol. 45, no. 6, pp. 1939–1953, Sep. 1999, doi: 10.1109/18.782116.
[21] Ö. Arslan and A. Tiemessen, "Adaptive bézier degree reduction and splitting for computationally efficient motion planning," *IEEE Trans. Robot.*, vol. 38, no. 6, pp. 3655–3674, Dec. 2022, doi: 10.1109/TRO.2022.3187296.
[22] T. Debarre, J. Fageot, H. Gupta, and M. Unser, "B-spline-based exact discretization of continuous-domain inverse problems with generalized TV regularization," *IEEE Trans. Inf. Theory*, vol. 65, no. 7, pp. 4457–4470, Jul. 2019, doi: 10.1109/TIT.2019.2902926.
[23] W. J. Gordon and R. F. Riesenfeld, *B-Spline Curves and Surfaces*. New York, NY, USA: Academic, 1974, pp. 95–126.
[24] S. Gao et al., "A B-spline method with AIS optimization for 2-D IoT-based overpressure reconstruction," *IEEE Internet Things J.*, vol. 7, no. 3, pp. 2005–2013, Mar. 2020, doi: 10.1109/JIOT.2019.2960827.
[25] D. Liu, D. Gu, D. Smyl, J. Deng, and J. Du, "B-spline level set method for shape reconstruction in electrical impedance tomography," *IEEE Trans. Med. Imag.*, vol. 39, no. 6, pp. 1917–1929, Jun. 2020, doi: 10.1109/TMI.2019.2961938.
[26] E. Eweda, N. J. Bershad, and J. C. M. Bermudez, "Stochastic analysis of the recursive least squares algorithm for cyclostationary colored inputs," *IEEE Trans. Signal Process.*, vol. 68, pp. 676–686, Jan. 2020, doi: 10.1109/TSP.2020.2964225.
[27] D. A. De Souza et al., "Identification by recursive least squares with Kalman filter (RLS-KF) applied to a robotic manipulator," *IEEE Access*, vol. 9, pp. 63779–63789, 2021, doi: 10.1109/ACCESS.2021.3074419.
[28] F. Tinazzi, P. G. Carlet, S. Bolognani, and M. Zigliotto, "Motor parameter-free predictive current control of synchronous motors by recursive least-square self-commissioning model," *IEEE Trans. Ind. Electron.*, vol. 67, no. 11, pp. 9093–9100, Nov. 2020, doi: 10.1109/TIE.2019.2956407.
[29] M. Unser, A. Aldroubi, and M. Eden, "B-spline signal processing. II. Efficiency design and applications," *IEEE Trans. Signal Process.*, vol. 41, no. 2, pp. 834–848, Feb. 1993, doi: 10.1109/78.193221.
[30] Z. Dong, C. Wu, X. Fu, and F. Wang, "Research and application of back propagation neural network-based linear constrained optimization method," *IEEE Access*, vol. 9, pp. 126579–126594, 2021, doi: 10.1109/ACCESS.2021.3111900.
[31] J. W. Zhang, S. B. Ye, H. Liu, L. Yi, and G. Y. Fang, "Filtering out antenna effects from GPR data by an RBF neural network," *IEEE Geosci. Remote Sens. Lett.*, vol. 16, no. 9, pp. 1378–1382, Sep. 2019, doi: 10.1109/LGRS.2019.2899896.
[32] B. Stappers, N. G. Paterakis, K. Kok, and M. Gibescu, "A class-driven approach based on long short-term memory networks for electricity price scenario generation and reduction," *IEEE Trans. Power Syst.*, vol. 35, no. 4, pp. 3040–3050, Jul. 2020, doi: 10.1109/TPWRS.2020.2965922.
[33] D. Shan, Y. Luo, X. Zhang, and C. Zhang, "DRRNets: Dynamic recurrent routing via low-rank regularization in recurrent neural networks," *IEEE Trans. Neural Netw. Learn. Syst.*, vol. 34, no. 4, pp. 2057–2067, Apr. 2023, doi: 10.1109/TNNLS.2021.3105818.
[34] Z. Jing, J. Liu, M. S. Ibrahim, J. Fan, X. Fan, and G. Zhang, "Lifetime prediction of ultraviolet light-emitting diodes using a long short-term memory recurrent neural network," *IEEE Electron Device Lett.*, vol. 41, no. 12, pp. 1817–1820, Dec. 2020, doi: 10.1109/LED.2020.3034567.
[35] F. Zhang, C. Hu, Q. Yin, W. Li, H.-C. Li, and W. Hong, "Multi-aspect-aware bidirectional LSTM networks for synthetic aperture radar target recognition," *IEEE Access*, vol. 5, pp. 26880–26891, 2017, doi: 10.1109/ACCESS.2017.2773363.
[36] N. Yang, J. Xiong, C. Guo, S. Guo, and G. Li, "Reflection coefficients inversion based on the bidirectional long short-term memory network," *IEEE Geosci. Remote Sens. Lett.*, vol. 19, Oct. 2022, Art. no. 3008605, doi: 10.1109/LGRS.2022.3216275.
[37] Z. Cui, N. Cui, J. Rao, C. Li, and C. Zhang, "Current distribution estimation of parallel-connected batteries for inconsistency diagnosis using long short-term memory networks," *IEEE Trans. Transp. Electrific.*, vol. 8, no. 1, pp. 1013–1025, Mar. 2022, doi: 10.1109/TTE.2021.3118691.

Peng Zhou (Senior Member, IEEE) received the B.S. degree in electronic engineering and the M.S. degree in automation control engineering from the China University of Petroleum, Dongying, China, in 1997 and 2000, respectively, and the Ph.D. degree in signal and information processing from the University of Electronic Science and Technology of China, Chengdu, China, in 2008.

He is an Associate Professor with the College of Oceanography and Space Informatics, China University of Petroleum, Qingdao, China. From 2017 to 2018, he worked as a Visiting Researcher with the Department of Information Engineering, University of Pisa, Italy. His current research interests include SAR imaging, ISAR imaging, and especially topics related to the radar imaging of ships.

Jichen Wu received the B.S. degree in electronic information science and technology from Shandong First Medical University, Tai'an, China, in 2022. He is currently working toward the M.S. degree in the College of Oceanography and Space Informatics, China University of Petroleum, Qingdao, China.

His current research interests include microwave imaging of ships.

Chuwen Cao received the B.S. degree in communication engineering from Ludong University, Yantai, China, in 2020, and the M.S. degree in information and communication engineering from the China University of Petroleum, Qingdao, China, in 2023, with the research topic as microwave imaging of ships.

Xi Zhang received the B.S. degree in information systems from the Qingdao University of Science and Technology, Qingdao, China, in 2005, and the M.S. degree in signal and information processing and the Ph.D. degree in computer science from the Ocean University of China, Qingdao, China, in 2008 and 2011, respectively.

In 2011, he joined the Laboratory of Marine Physics and Remote Sensing, the First Institute of Oceanography (FIO), Ministry of Natural Resources of China, Qingdao. Since 2021, he has been a Professor with FIO. Since 2020, he has been with the supervisor of doctoral students with China University of Petroleum. He is a guest editor (special issue) for IEEE GEOSCIENCE AND REMOTE SENSING MAGAZINE and *International Journal of Applied Earth Observation and Geoinformation*. He has authored more than 100 journal and conference papers, has written one book as a coauthor, and won five Chinese provincial and ministerial awards. His research interests include radarsignal processing, SAR target detection, and marine and cryosphere environment remote sensing.

Dr. Zhang is a member in the Specialized Committee on Artificial Intelligence Oceanography of the Ocean Society of China and the Working Committee on Marine Spatial and Temporal Information of the China Association of Geoinformation Industry.

Zhenhua Zhang received the Ph.D. degree in signal processing from Xidian University, Xi'an, China, in 2007.

He is currently a Professor with the School of Astronautics, Beihang University, Beijing, China. His current research interests include SAR imaging and radar signal processing.

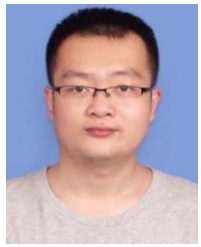

Genwang Liu received the B.S. and M.S. degrees in automation from Inner Mongolia University, Hohhot, China, in 2011 and 2014, respectively, and the Ph.D. degree in computer science from the Ocean University of China, Qingdao, China, in 2017.

He is currently a Research Associate with the Laboratory of Marine Physics and Remote Sensing, First Institute of Oceanography, Ministry of Natural Resources, Qingdao. His research interests include ship synthetic aperture radar (SAR) detection and classification, polarimetric SAR and marine applications, and SAR simulation and image interpretation.

Jie Zhang received the B.S. and M.S. degrees in mathematics from Inner Mongolia University, Hohhot, China, in 1984 and 1987, respectively, and the Ph.D. degree in applied mathematics from Tsinghua University, Beijing, China, in 1993.

He is the Dean of the College of Oceanography and Space Informatics, China University of Petroleum, Qingdao, China. His research interests include SAR retrieval of ocean dynamics processes and SAR detection of marine targets, ocean hyperspectral remote sensing, ocean detection techniques utilizing high-frequency surface wave radar, and the integration of marine remote sensing application systems.